Upcycling of Paper Waste for High-performance Lithium-Sulfur Batteries

Yucheng Zhou [a], Yunya Zhang [a], Xiaodong Li [a], *

[a] Department of Mechanical and Aerospace Engineering, University of Virginia, 122 Engineer's Way, Charlottesville, VA 22904-4746, United States.

* Corresponding Author. E-mail: xl3p@virginia.edu

Abstract: Fast-expanding electric vehicle market demands eco-friendly, high-performance, and low-cost energy storage systems. Lithium-sulfur battery with higher theoretical specific capacity and lower cost is regarded as a promising successor to lithium-ion battery. However, lithium-sulfur battery's polysulfide shuttling and lithium degradation have hindered its practical applications. In this study, cellulose fibers were extracted from recycled paper hardboards by a simple alkaline treatment and then coated onto polypropylene separators by vacuum filtration. When being used as lithium-sulfur battery separators, the negatively charged functional groups on the cellulose fibers repelled polysulfide-ions and redistributed lithium-ions, enabling the assembled cells superior stability and long lifespan. The lithium-sulfur battery with the recycle paper cellulose fiber coated separator exhibited a lifespan of over 800 cycles with a capacity retention rate of 71.69 % and nearly no capacity decay after the initial formation cycles. The finding demonstrates that renewably-produced, cellulose fiber-coated polypropylene separators can simultaneously reduce the shuttle effect and degradation of lithium, paving the way towards commercially-viable and environmentally-friendly lithium-sulfur batteries.

Keywords: Cellulose fiber, recycled paper, lithium-sulfur battery, separator, sustainability

1. Introduction

Over the past several decades, energy crises and environmental issues have grown into worldwide problems. To overcome the problems, an ever-growing number of sustainable and eco-friendly materials have been explored for efficient and renewable energy storage. Among them, cellulose fiber (CF), a type of natural polymers, has received extensive attention due to their abundance and wide applications in daily supplies, such as newspapers and paper containers [1, 2]. Although CFs are used in many everyday products, they are not recycled at a very high rate [3]. Purified crystalline CFs have the potential to be employed in high value-added applications, such as natural fiber-reinforced thermosets, thermoplastic composites. Moreover, CF-reinforced separators can be used in lithium-ion (Li-ion) batteries, which are currently the most common energy-storage devices [4-9].

Replacing combustion engines with high-energy batteries is considered to be an effective route to reduce the consumption of fossil fuel and pollutant emissions [9]. However, after years of optimization, the Li-ion battery is approaching its theoretical energy density limit. Electric vehicles that utilize Li-ion batteries will always be restricted in their range by this theoretical limit. In order to increase the effective range of electric vehicles, the energy density of batteries needs to be increased past the theoretical maximum of Li-ion based systems. The lithium-sulfur (Li-S) battery is a promising alternative for replacing current Li-ion battery due to its high theoretical specific capacity (1,675 mAh g^{-1}) and energy density (2,600 Wh kg^{-1}) [10-14]. Li-S batteries are also constructed with inexpensive raw materials. Nevertheless, the

practical application of Li-S batteries is hindered by two major challenges: the soluble polysulfides' shuttle effect, which leads to self-discharging, and the growth of mossy Li, arising from nonhomogeneous distribution of Li-ions [15-18]. To overcome the current challenges that prevent Li-S batteries from commercialization, all components in the battery must be systematically optimized. Although the anode, cathode, and electrolyte of Li-S batteries have been researched extensively, the separator has been largely overlooked until recently [19-21]. For example, Yao *et al.* [22] reported on directly coating a thin porous carbon layer onto the separator, rendering the Li-S battery with an initial specific capacity of 1,350 mAh g^{-1}, a lifespan of over 500 cycles at 0.5 C, and a capacity decay rate as low as 0.09 % per cycle. In addition to coating, another strategy to enhance separator's efficacy is introducing interlayers between separators and electrodes [23, 24]. These studies indicate that battery performance can be largely enhanced by modifying the separator. However, introducing interlayers increases the overall thickness of the battery, leading to reduced volume energy density and increased ion transport distance. Most recently, studies on carbon- and polymer-based separator coatings and interlayers have been mainly focusing on polysulfide trapping mechanism via various methods such as nitrogen doping and carbon functionalization [25-30]. This helps mitigate the migration of polysulfides to reach the anode by trapping polysulfides in coating layers or interlayers; however, it inevitably increases the irreversible waste of active materials because some of them are anchored in those layers. Besides, in order to reduce the cost of the synthesis process, new cost-effective raw materials with simple manufacturing strategies are much needed.

The CFs from recycled paper are capable of being manufactured and functionalized as effective additives to enhance separators. Unlike current separators in Li-S batteries, recycled paper is low-cost and readily available. In past research, we used activated paper carbon (APC) with graphene and sulfur as the cathode and a piece of APC as an interlayer between the separator and anode in the Li-S battery to prevent the growth of mossy Li, which led to a stretch of lifespan up to 1,000 cycles with a capacity retention rate of 52.3 % [31]. This created a new possibility to obtain high-performance full Li-S batteries from biomass materials containing CFs. Our previous study indicates that high-temperature treated CF-based biomass materials as interlayers in Li-S batteries can redistribute Li-ions [31]. This effectively prevents the growth of mossy Li. Furthermore, negatively charged functional groups on CFs are expected to mitigate the shuttle effect by repelling soluble polysulfides [32-34]. Unlike the trapping mechanism, this concept reduces the polysulfide shuttle effect without sacrificing active materials. Hence, high-purity CFs are a promising material that may simultaneously mitigate the shuttle effect and mossy Li growth in Li-S batteries.

Here, the CFs extracted from paper waste were uniformly coated onto commercial polypropylene separators on the cathode side when being assembled into Li-S batteries with an APC/S cathode. It was found that the functional groups on the CFs, such as carboxylic groups and phenolic groups, tended to lose their H^+ ions and form a negatively charged surface, which simultaneously repelled the anionic polysulfides (S_x^{2-}) and redistributed the cationic Li-ions (Li^+) during battery operation (Figure 1). This led to a joint improvement of rate ability, lifespan, and capacity retention rate. This

waste-to-wealth approach employed low-cost CFs to simultaneously prevent the polysulfide shuttle effect and nonhomogeneous Li degradation, paving the way towards commercially viable Li-S batteries.

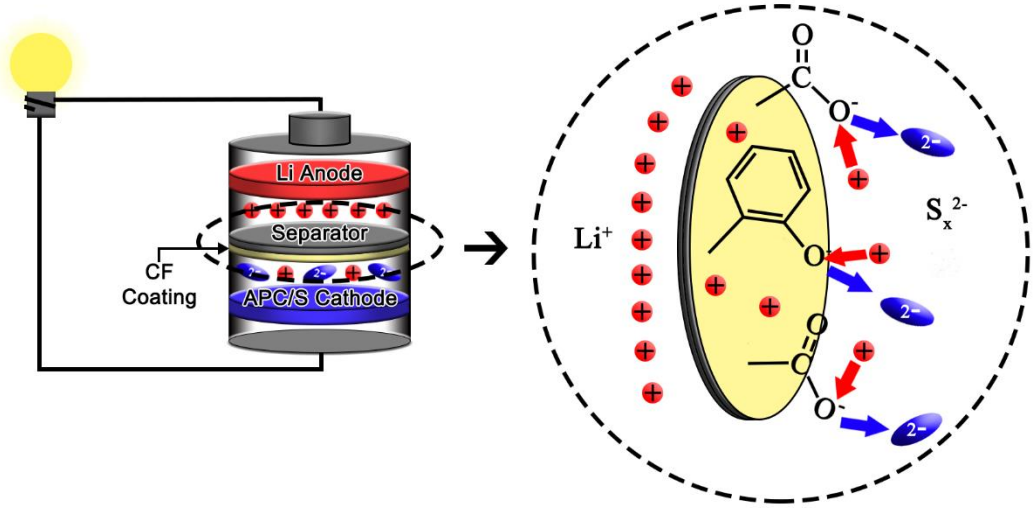

Figure 1. Schematic of the CF-coated separator repelling polysulfide-ions and redistributing Li-ions.

2. Experimental Section

2.1 CF extracting process

A piece of 65 x 50 mm rectangular hardboard was cut into pieces. The 5 wt.% sodium hydroxide (NaOH) solution was stirred with the paper pieces at room temperature, and then the suspension was held at 80 °C for 3 hours. Sonicating was performed to further disperse the CFs after the alkaline treatment. The centrifugation was used three times in DI water and twice in isopropyl alcohol at a rate of 3500 rpm for 10 minutes. Eventually, the isopropyl alcohol was added to preserve the suspension in an organic solution condition.

2.2 CF coating process

The Celgard 2400 separators were cut into rectangular pieces. Vacuum filtration was applied to coat the CFs onto the surfaces of the separators. The coated separators were then dried at 60 °C for 12 hours.

2.3 Battery assembling

The dried CF-coated separators were punched into circular pieces for coin cells. The electrolyte was produced by dissolving 1 mol L^{-1} lithium bis(trifluoromethanesulfony)imide (LiTFSI) and 0.4 mol L^{-1} $LiNO_3$ in an organic solvent of dimethoxyethane (DME) + 1,3-dioxolane (DOL) at a 1:1 volume ratio. The electrolyte for each battery was 16 μL. An activated paper carbon with sulfur (APC/S) was employed as the electrode. To prepare the APC/S, thin pieces of hardboards were first punched into round pieces and heat-treated in a tube furnace at 1,000 °C for one hour with argon. The APC pieces were then loaded sulfur powders, following by a heat treatment at 155 °C for 12 hours and at 200 °C for 2 hours to impregnate sulfur and form the APC/S pieces to be directly used as cathodes. The areal mass loadings of APC/S cathodes in the CF-enabled battery and non-CF battery were 5.15 mg cm^{-2} and 5.38 mg cm^{-2}, respectively. The APC/S cathodes, separators, electrolytes, and Li anodes were assembled into coin cells manually.

2.4 Battery disassembling

In order to observe polysulfide distribution, the batteries were in charged condition, disassembled manually in the glove box with argon. Failed batteries were also disassembled manually to conduct a post-failure study. The cycled cathodes, anodes

and separators were collected separately for inspection without further treatment.

2.5 Permeation experiment

Shredded Li metal pieces and sulfur powders with an atomic ratio of 1:3 were added to a beaker filled with electrolytes. The mixture was stirred at a temperature of 60 °C for 48 hours to obtain the Li_2S_6 solution. The solution was separately added into two small glass tubes attached to the lids with 1 mL for each. The glass tubes were then covered separately by an uncoated separator or a CF-coated separator and sealed in two vials filled with electrolyte. The whole experiment was conducted in a glove box filled with Ar.

2.6 Density functional theory calculation

The QUANTUMESPRESSO software package was employed to perform the DFT calculations with a norm-conserving pseudopotential and with the SCAN meta-GGA exchange-correlation functional [35, 36]. A gamma k-point mesh was used and the kinetic energy cutoffs for the wave function and charge density were 30 and 300 Ry, respectively. The models were relaxed using the Broyden-Fletcher-Goldfarb-Shanno (BFGS) quasi-Newton algorithm [37].

2.7 Materials and Structural Characterization

The SEM (FEI Quanta 650 with EDS detector), XRD (Empyrean Multipurpose X-ray Diffractometer equipped with Cu Kα radiation (λ = 0.15406 nm)), and XPS (PHI Versaprobe III Scanning XPS with Processing Chamber and Reaction Cell) were employed to characterize the as-prepared APC/S cathodes, CF layers, separators, and Li anodes.

2.8 Electrochemical Characterization

A LAND CT2003A battery test instrument was used to conduct galvanostatic charge/discharge measurements, including cyclic performance, polarization voltage, and rate performance. The polarization voltage was calculated using the following equation in the test station

$$V_p = V_t - IR_0 - V_{oc} \quad (1)$$

where V_p is the polarization voltage, V_t is the terminal voltage, I is the current, R_0 is the ohmic resistance, and V_{oc} is the open-circuit voltage, which were measured by the test station. A CHI 660E electrochemical workstation was used to conduct the EIS test in the frequency range from 100 kHz through 0.01 Hz with an AC perturbation of 5 mV, as well as the CV test from 1.5 V to 2.8 V with a scan rate of 0.0001 V s^{-1}. The Zview software was applied to perform the curve-fitting on the EIS test data.

3. Results and Discussion

3.1 Characterization of CF-coated separator:

The process regarding the fabrication of CF-coated separators is illustrated in Figure S1 (Supporting information). The CF suspension (Figure 2b) was extracted from a used hardboard (the inset of Figure 2a) through an alkaline treatment, and coated onto a Celgard 2400 polypropylene separator (the inset of Figure 2c) via vacuum filtration. The CF coating weighed 1.3 mg (0.56 mg cm^{-2}), which was the most optimal CF loading. With lower or higher loading of CFs, consequences that the repelling phenomenon was weak or the CFs partially blocked the route for ion exchanging would

occur, respectively. The CFs (Figure 2c) exhibit a cross laid fiber surface with an average length of more than 1 mm (Figure S2) and width of nearly 18 μm, enabling Li-ion transport through the separator. The thickness of the CF coating was measured to be 47.18 μm on average (Figure 2d). Energy-dispersive X-ray Spectroscopy (EDS) mapping showed carbon (Figure 2e) and oxygen (Figure 2f) on the CF coating. X-ray Diffraction (XRD) was performed on the recycled paper and CF coating (Figure 2g). The broad peaks in the 2θ range of 14.0 ° to 16.0 ° and at 22.5 ° match the characteristic peaks of the typical cellulose I (native cellulose) [38]. The peaks at 12.5 °, 25 °, and 27.5 ° correspond to kaolin ($Al_2Si_2O_5(OH)_4$) and the peak at 29.5 ° is characteristic of calcium carbonate ($CaCO_3$) [39, 40]. Both of these compounds are often used as additives in the production of paper products [41]. The alkaline treatment and coating process eliminated most of the impurities, except for a small amount of $CaCO_3$ (1.2 wt%), which should have little impact on the electrochemical reaction [42, 43]. X-ray photoelectron spectrometer (XPS) inspection unveiled a small Ca2p peak (Supporting information, Figure S3a), which is in good agreement with the XRD results. The three peaks with binding energies of 288.14 eV, 286.56 eV and 284.77 eV (Figure 2h) are from the carboxylic (-COOH) group, phenolic (-C-OH) group, and aromatic (C=C) group, respectively [44, 45]. This is consistent with the O1s spectrum (Figure 2i), where a large peak is located at a binding energy of 533.10 eV (representing co-existence of the -COOH and -C-OH groups), while a small peak at 531.22 eV corresponds to the C=O group [44, 46]. The -COOH and -C-OH groups easily lose their H^+ ions, which enables the separator surface facing the cathode to become negatively charged [32, 47,

48]. The negatively charged surface is expected to repel the anionic S_x^{2-} and attract the cationic Li^+. Consequently, this reduces the shuttle effect of polysulfides, increases the efficiency of the Li-ion exchange, and promotes uniform ion distribution [32, 34]. On the other hand, although nitrogen (N) -containing functional groups were detected in the raw recycled paper, no N-related functional groups were observed on the surface of the CF-coated separator (Figure S3b) due to the alkaline treatment using NaOH [32]. This rules out the possibility that the CF layer traps polysulfide-ions [49]. Therefore, the negatively charged surface was able to repel soluble polysulfides during battery operation, rendering the active materials fully usable.

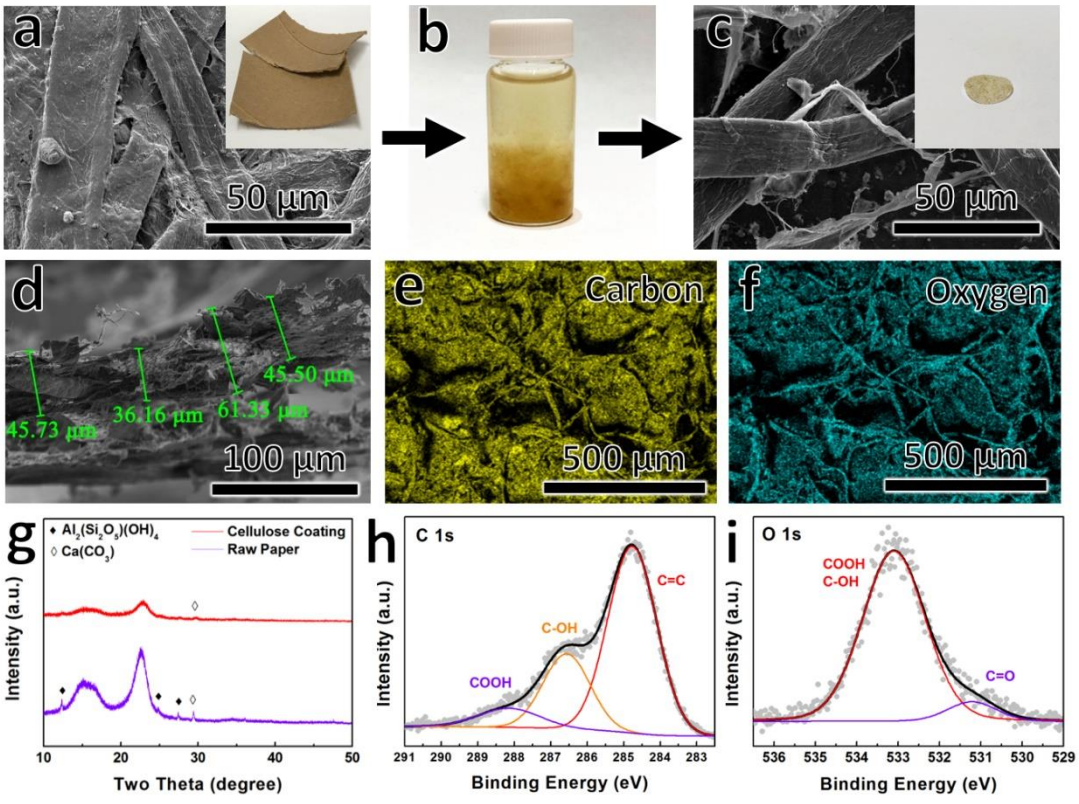

Figure 2. (a) SEM image of a paper hardboard. The inset shows the optical image of the hardboard. (b) CF suspension in ethanol. (c) SEM image of the CF-coated separator. The inset shows the optical image of the CF-coated separator. (d) SEM image of the CF coating cross

section. (e) EDS map of carbon. (f) EDS map of oxygen. (g) XRD spectra of the hardboard and CF coating. (h) C1s spectrum on the CF coating. (i) O1s spectrum on the CF coating.

3.2 Simulation and experiment of functional groups on polysulfides:

Density functional theory (DFT) calculations were used to validate the repelling mechanism of the CF functional groups. The S_8^{2-} and S_6^{2-} chain model was built and placed in the front of the $-COO^-$ (Figure 3a and c) group and $-C-O^-$ (Figure 3b and d) group models which were connected to fixed benzene models. All models were relaxed separately before calculation to ensure accuracy. The DFT simulations demonstrate that both carboxylic and phenolic groups without H^+ repel the S_8^{2-} and S_6^{2-} chains to achieve lower total energy. Figure 3a shows that the distances between atom 1 (the oxygen) and atom 2 (the nearest sulfur), and atom 1 and atom 3 (the second nearest sulfur) increased from 2.011 Å to 2.976 Å, and 2.191 Å to 2.207 Å, respectively. While the distances, in Figure 3b, between atom 1 (the oxygen) and atom 2 (the nearest sulfur), and atom 1 and atom 3 (the second nearest sulfur) increased from 2.070 Å to 2.861 Å, and 2.343 Å to 2.736 Å, respectively. Similar results regarding the functional groups repelling S_6^{2-} can be also observed. Figure 3c reveals that the distances between atom 1 (the oxygen) and atom 3 (the nearest sulfur), and atom 1 and atom 2 (the second nearest sulfur) increased from 2.363 Å to 2.591 Å, and 2.706 Å to 2.802 Å, respectively. Moreover, the distances, in Figure 3d, between atom 1 (the oxygen) and atom 2 (the nearest sulfur), and atom 1 and atom 3 (the second nearest sulfur) increased from 2.223 Å to 2.751 Å, and 2.939 Å to 2.962 Å, respectively. To visualize the repelling mechanism, a comparison between

polysulfides (mostly Li_2S_6) permeated through an uncoated separator or a CF-coated separator was exhibited with time (Figure 3e). The result showed that the polysulfides permeated faster through the uncoated separator than the CF-coated separator, indicating that the CF-coated separator partially repelled the polysulfides. Both the DFT calculations and permeation experiment demonstrate that the functional groups enable the polysulfide-ion repelling mechanism, which mitigates the shuttle effect without consuming active materials.

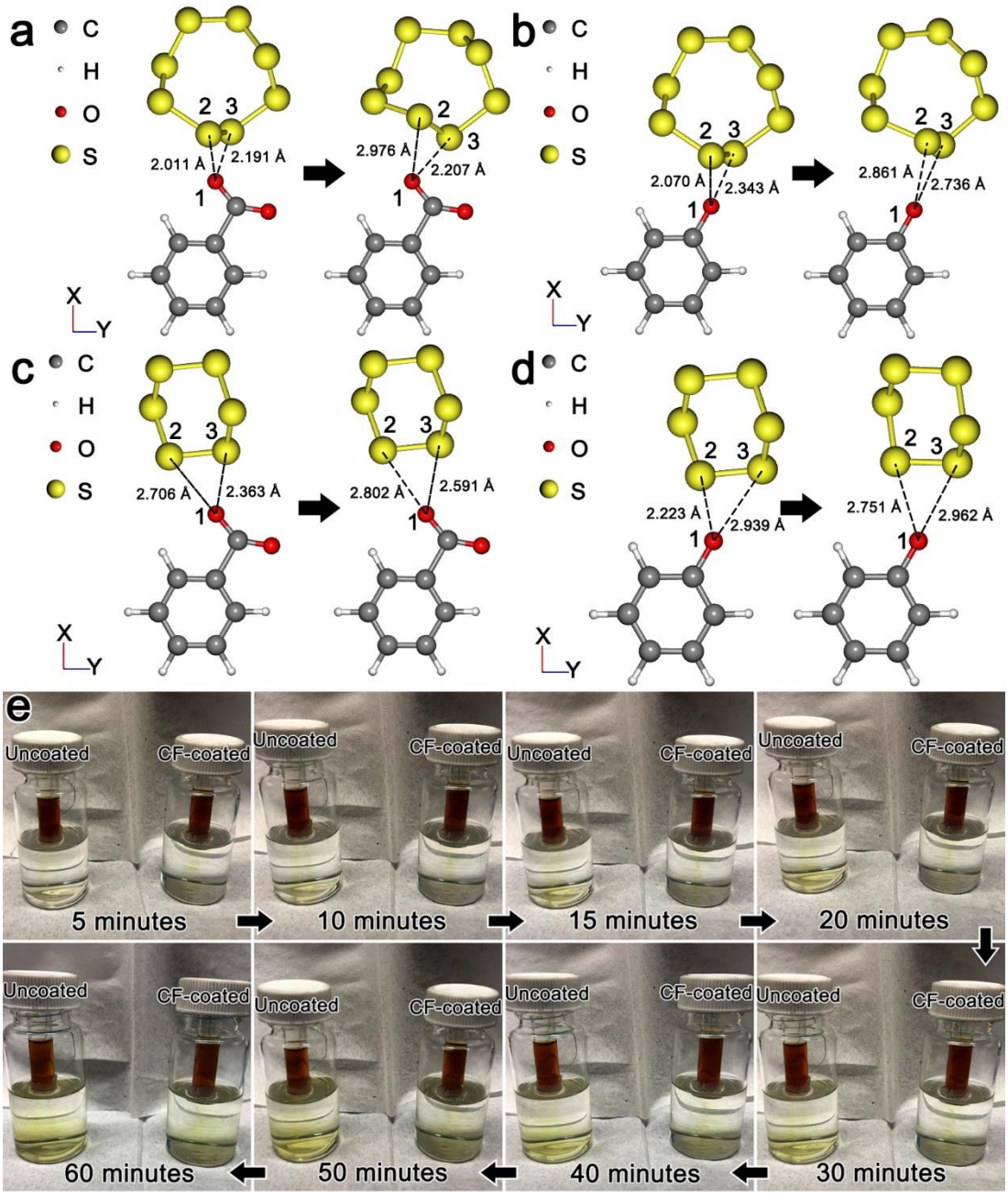

Figure 3. (a) DFT simulation of the carboxylic group on S_8^{2-} polysulfides. (b) DFT simulation of the phenolic group on S_8^{2-} polysulfides. (c) DFT simulation of the carboxylic group on S_6^{2-} polysulfides. (d) DFT simulation of the phenolic group on S_6^{2-} polysulfides. (e) Permeation experiment between the uncoated separator and CF-coated separator after 5 minutes, 10 minutes, 15 minutes, 20 minutes, 30 minutes, 40 minutes, 50 minutes, and 60 minutes.

3.3 Electrochemical performance of CF-enabled batteries:

The CF-coated separator was used to construct the Li-S battery with APC/S as the cathode and Li as the anode. Figure 4a shows the typical charge/discharge cycle (0.16 C) of the CF-coated separator enabled battery. During discharging, four stages (I to IV) appeared and can be ascribed to the formation of S_8^{2-} (stage I), change from S_8^{2-} to S_6^{2-} and S_4^{2-} (stage II), transformation from S_4^{2-} to Li_2S_2 (stage III), and formation of Li_2S solid (stage IV), respectively. The charge curve, similarly, can be grouped into three stages (V to VII), which are ascribed as the change from the solid Li_2S to low-order polysulfides (stage V), conversion from low-order to high-order polysulfides (stage VI), and solidification from high-order polysulfides back to the solid sulfur (stage VII). Comparing with the non-CF battery (Figure S4a), the CF-enabled battery had a flatter plateau at stage I and a much broader and flatter plateau at the stage III in the discharge segment, as well as a flatter plateau at stage VII in the charge segment. These indicate that a large number of polysulfides were repelled, remaining at the cathode side for electrochemical reaction. The faster decrease of the potential at stage IV of the CF-enabled battery also supported the conclusion. Moreover, the CF-enabled battery had a larger potential gap between the charge curve and discharge curve. This is further analyzed in the electrochemical impedance spectroscopy (EIS) section.

Cyclic voltammetry (CV) curves collected after the 0^{th} cycle, 5^{th} cycle, 50^{th} cycle, and 200^{th} cycle are plotted in Figure 4b. The CV curves with cycle numbers of the CF-enabled battery were consistent with the typical values and similar to the non-CF battery (Supporting information, Figure S4b) after the initial cycle, indicating that the CF layer

was stable without significant changes under electrochemical reaction condition [50]. For the cathodic scan, two sharp troughs, troughs (1) and (2), appeared to represent the two plateaus (stages I and III) in the typical charge/discharge cycle. Similarly, for the anodic scan, the broad peak (3) at 2.5 V indicated that the Li_2S fully transformed into S_8^{2-}, corresponding to the broad plateau (stage VII) in the charge/discharge cycle. During cycling, the trough (1) moved to a higher potential, and after the 50^{th} cycle, the CF-enabled battery became stabilized. When the battery reached the 200^{th} cycle, the intensity of trough (1) became higher in the discharge scan, which represents the transformation from S_4^{2-} to S_2^{2-} and S^{2-}, indicating developing mitigation of the shuttle effect. For comparison, charge/discharge curves after the 0^{th} cycle, 5^{th} cycle, 50^{th} cycle, and 200^{th} cycle were also obtained from the non-CF battery (Supporting information, Figure S4b), where no substantial difference was observed until the 50^{th} cycle, and hereafter, similarly, a developing intensity of trough (1) was detected. The potential difference between trough (2) and peak (3) in the CF-enabled battery was larger than that in the non-CF battery.

To further study the electrochemical performance of the CF-enabled battery, EIS measurements were carried out on both CF-enabled and non-CF batteries. Except for the impedance curve from the 0^{th} cycle, two semicircles and a straight line emerged in the high-frequency regime, intermediate-frequency regime, and low-frequency regime, respectively (Figure 4c). The semicircles and the straight line can be further described as an equivalent circuit (the inset of Figure 4c). The intercept between the semicircle in the high-frequency regime and Z' axis is equal to the R_I in the circuit, denoting the

equivalent series resistance R_{Ω}. The semicircle in the high-frequency regime is the impedance of ions traveling through the solid-electrolyte interface (SEI) of the anode and electrolyte. This semicircle can be represented by a resistor and a capacitor in the equivalent circuit where the resistor is noted as R_{II} (or R_{int}) and can be calculated by the diameter of the semicircle. The second semicircle at the intermediate-frequency regime is known as the impedance of the charge exchanging between the electrodes and electrolyte, which also can be described as a resistor R_{III} (also known as R_{CT}) and a capacitor in the equivalent circuit. The straight line in the low-frequency regime is the Warburg impedance and can be derived from an ion-diffusion limited condition in the electrolyte, written as Z in the circuit. During cycling, the overall impedance of the CF-enabled battery decreased gradually. In contrast, the total impedance of the non-CF battery (Supporting information, Figure S4c) decreased rapidly after the first cycle and then increased with further cycling.

Another intriguing property of the CF-enabled battery is its rate ability. The rate performance tests were carried out on the batteries after stabilization (Figure 4d). It was shown that with the CF coating layer, the rate ability of the battery could still be maintained at a high level, which was even slightly better than the non-CF battery. More specifically, the CF-enabled battery exhibited a good capacity retention rate of 72.43 % from 744.29 mAh g^{-1} to 539.12 mAh g^{-1} when the operation rate was octupled from 0.16 C to 1.28 C, while the non-CF battery showed a retention rate of 70.14 % from 754 mAh g^{-1} to 528.84 mAh g^{-1} with the same operation rate increase. The higher capacity retention rate of the CF-enabled battery was attributed to the repelling

mechanism induced by the functional groups on the CFs, which kept more polysulfides at the cathode side. This allowed the relatively more polysulfides to be reacted at a high operation rate. When the operation rate returned to 0.64 C, the specific capacities of both the CF-enabled battery and non-CF battery were fully recovered.

The CF-enabled battery with a sulfur load of 3.1 mg cm^{-2} (60.2 wt%) cycled over 800 times at the rate of 0.5 C. An initial discharge capacity of 1,016.0 mAh g^{-1} (3.15 mAh cm^{-2}) (Figure 4e) was attained. For comparison, the cyclic performance of the non-CF battery using an APC/S cathode with a sulfur load of 3.3 mg cm^{-2} (61.3 wt%) was also measured. Figure 4e reveals that the capacity decay of the first cycle in the CF-enabled battery was 33.2 %; the retention rate at the 800^{th} cycle was 71.69 % (nearly 0.035 % capacity decay per cycle); and more importantly, there was almost no capacity fading after the initial two cycles. For comparison, the non-CF battery exhibited a capacity decay of 39.6 % after the first cycle, which is 19.3 % larger than that of the CF-enabled battery. The first cycle decay of a Li-S battery is often induced by the SEI layer formation, causing the irreversible capacity decrease and unusable sulfur formation [51, 52]. Therefore, the CF-reinforced separator can prevent more polysulfide-ions from passing through due to the repelling mechanism of the functional groups than the uncoated separator. In addition, the much smaller overall capacity decay and more stable cyclic performance were also attained in the CF-enabled battery with the assistance of the CF-coated separator. It is worth mentioning that the non-CF battery failed after cycling 466 times, which is much shorter than the lifespan of the CF-enabled battery (over 800 times). The stable cycling performance with the long lifespan of the

CF-enabled battery is also better than that of the recent Li-S batteries with similar coatings or interlayers (Supporting information, Table S1) [25, 26, 28]. The higher capacity of the non-CF battery in the initial cycles was mainly due to the lower impedance in the non-CF battery at the beginning [51, 53]. With the impedance increase of the non-CF battery and the impedance decrease of the CF-enabled battery during cycling, the specific capacity of the CF-enabled battery exceeded that of the non-CF battery. The Coulombic efficiency was close to 100 % in the CF-enabled battery. Due to the excess Li metal anode, the capacity retention rate maintained at 71.69 % after 800 cycles even with the Coulombic efficiency lower than 100 %. After the 350^{th} cycle, the Coulombic efficiency started decreasing, yet it was above 93 % until failure.

Polarization voltages of the CF-enabled battery and non-CF battery were calculated to describe the polarization characteristics in the batteries during cycling (Figure 4f). Curve fitting was performed to numerically analyze the variation trend. A large polarization voltage of 672.1 mV was found in the first cycle of the non-CF battery. It then drastically decreased to 496.5 mV in the second cycle, and gradually increased to 667.3 mV up to the 466^{th} cycle. Surprisingly, the CF-enabled battery only experienced an initial polarization voltage of 293.9 mV. It then rapidly decreased to 206.2 mV in the second cycle, and gradually increased to 363.4 mV until the 800^{th} cycle. The much smaller polarization voltage and increasing trend of the CF-enabled battery jointly indicate that the polarization was much lower in the CF-enabled battery than that of the non-CF battery.

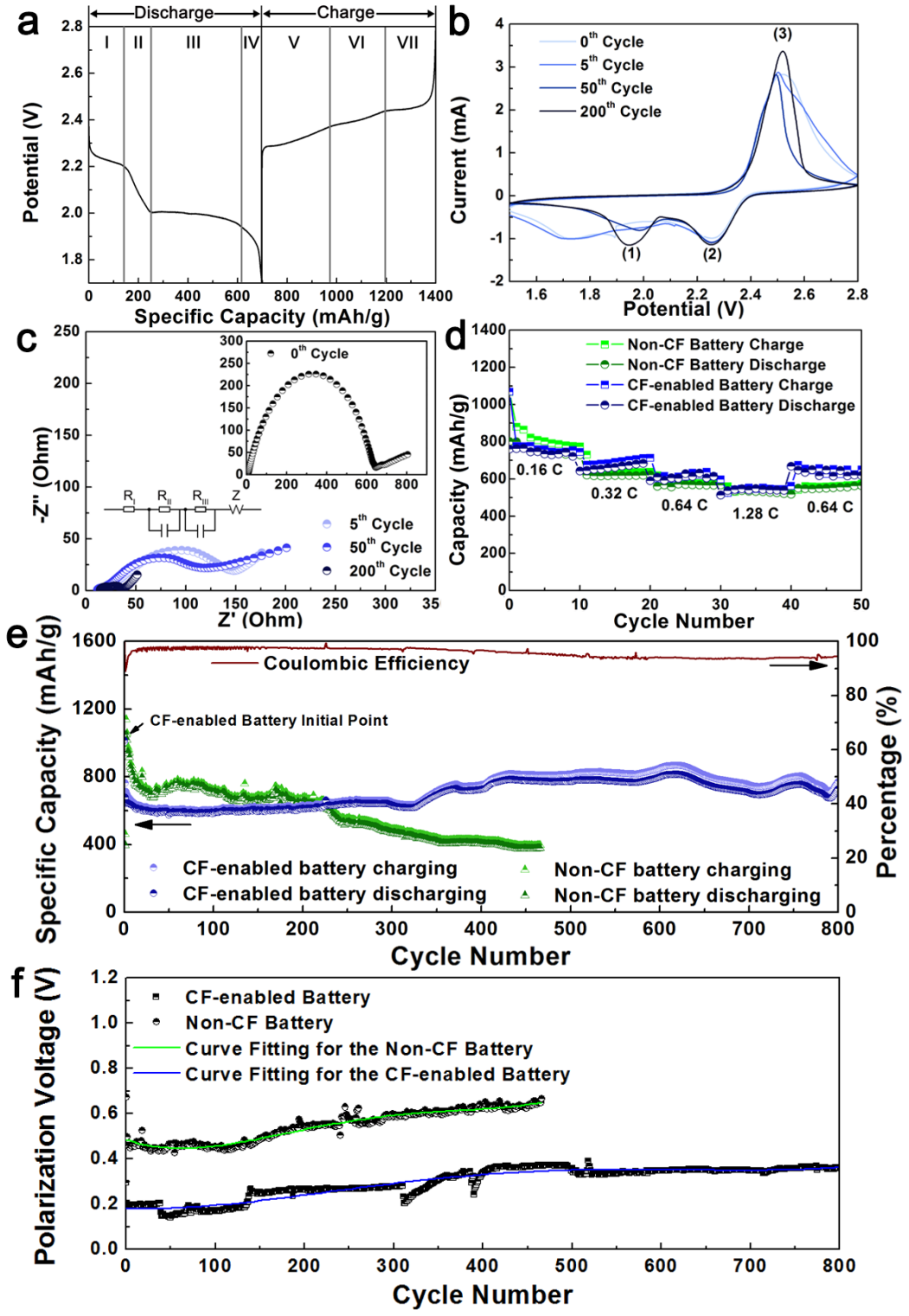

Figure 4. (a) Typical charge/discharge cycle of the CF-enabled battery. (b) CV curve of the CF-enabled battery. (c) EIS curve of the CF-enabled battery. The insets show the EIS curve of the battery before cycling and equivalent circuit of the EIS data. (d) Rate performance of the CF-enabled battery and non-CF battery. (e) Overall cyclic performance of the CF-enabled battery

with the areal cathode mass of 5.15 mg cm^{-2} and non-CF battery with the areal cathode mass of 5.38 mg cm^{-2}. (f) Polarization voltage of the CF-enabled battery and non-CF battery.

3.4 Analyses of impedance and polarization

To quantitatively analyze the impedance variation with the cycle number, curve fitting (Supporting information, Figure S5) was employed using Zview with the fitting model same as the circuit inset in Figure 4c. Comparing the two data sets (Table 1), the series resistance R_Ω of the CF-enabled battery is slightly larger than that of the non-CF battery due to the introduction of the negatively charged CF layer. This explains the slightly larger gap of potential between the charge and discharge curves in the typical charge/discharge cycle analysis section, and the larger potential difference between the trough (2) and peak (3) in the CV analysis section of the CF-enabled battery than those of the non-CF battery. In accordance with the fitting data, high resistance was obtained, which corresponds to the semicircles at the high-frequency regime in both the CF-enabled battery (565.8 Ω) and non-CF battery (203.3 Ω) before cycling, which suggests the existence of oxidized layers on the Li anodes. This impeded the Li-ion transport in the battery. These values decreased drastically and remained low after the first cycle as the oxidized layers were removed. Upon cycling (the end of the 5^{th} cycle), the larger R_{int} in the CF-enabled battery (19.37 Ω) than that in the non-CF battery (3.74 Ω) represented a faster formation of the SEI layer. As the cycling proceeded, the CF-enabled battery exhibited a decreasing trend of the R_{int}, while the R_{int} of the non-CF battery increased and then stabilized. The reduction of R_{int} in the CF-enabled battery

may ascribe to the extra kinetic energy from the negatively charged CF layer on particles, such as Li-ions during charging and electrons during discharging. This energy accelerated particle transport, which gradually weakened the formation of SEI layers. In addition, the higher R_{CT} in the CF-enabled battery (101.8 Ω) than that in the non-CF battery (13.19 Ω) at the end of the 5th cycle could arise from the inactive CF layer introducing an impedance layer at the beginning, which decreased the electrically conductive area [51]. However, as the CF layer being activated during cycling (losing H^+ ions), the R_{CT} decreased rapidly because the negatively charged layer repelled the anions and accelerated the transport of cations. Therefore, the side reactions between the cations and anions were decreased, leading to an increasingly thinner impedance layer formed on the electrode. This decreasing trend can also explain the increasing specific capacity after the initial cycles and the trough (1) in the CV curve moving to a higher potential [50, 51, 54]. In contrast, the absence of the CF layer in the non-CF battery induced a cumulative impedance layer, leading to an increase in R_{CT} and a consecutive decay in capacity [51].

Table 1. Curve fitting data of the EIS test.

	Non-CF Battery				CF-enabled Battery			
	0th Cycle	5th Cycle	50th Cycle	200th Cycle	0th Cycle	5th Cycle	50th Cycle	200th Cycle
R_{Ω} (Ohm)	2.987	9.083	7.782	8.71	2.419	11.09	10.1	13.55
R_{SEI} (Ohm)	203.3	3.74	18.02	20.33	565.6	19.37	16.2	9.986
R_{CT} (Ohm)	288.1	13.19	54.17	183	-	101.8	50.2	12.51

Due to the introduction of the negatively charged functional group layer on the separator, the potential balance in the battery was maintained to a certain degree,

leading to a smaller polarization. To better understand the polarization mechanism, the expression for polarization provided by the separator [55] can be formulated as

$$E^{\Delta s} = E_1^{\Delta s} + E_2^{\Delta s} = \frac{1}{j_{appl}}\left[\int_0^{L^s}\left(\frac{j_L^2}{\kappa_{eff}}\right)dx - \int_0^{L^s} j_L \cdot \frac{2RT}{c_L F}\kappa_c \frac{\partial c_L}{\partial x}dx\right] \quad (2)$$

where $E^{\Delta s}$ is the polarization of the separator, $E_1^{\Delta s}$ is the polarization caused by the ohmic potential drop, $E_2^{\Delta s}$ is the diffusion polarization , j_{appl} is the applied current density, L^s is the thickness of the separator, j_L is the current density in electrolyte, κ_{eff} is the effective ionic conductivity accounting for the porosity and tortuosity, R is the ideal gas constant, T is the temperature, c_L is the concentration in the electrolyte, F is the Faraday's constant, and κ_c is the concentration conductivity. Because the two batteries were cycled in the same conditions, and the only difference between them was the CF layer, we can consider that j_{appl}, L^s, j_L and T are invariant. The ionic conductivity κ_{eff} can be calculated from the following equation [56, 57]

$$\kappa_{eff} = \frac{d}{A \cdot R_e} \quad (3)$$

where *d* is the thickness of electrolyte, *A* is the contact area, and R_e is the resistance of the electrolyte. *d* can be obtained by measuring the thicknesses of the separator and coating layer, *A* is the area of the separator, and R_e can be obtained from the intercept of Z' axis and the regression of the straight line (denoting the Warburg impedance) derived from an ion-diffusion limited condition in the EIS data. To obtain R_e, two batteries with only electrolyte and a CF-coated separator or an uncoated separator were separately built. From the regression of the EIS results (Figure S4d), the R_e of the CF-coated separator battery was calculated to be 2.028 Ω, while the R_e of the non-CF

separator battery was calculated to be 4.658 Ω. With *d* of 67.18 μm for the CF-coated separator and 20 μm for the uncoated separator, and *A* value of 3.1416 cm^2 for both batteries, κ_{eff} values of the CF-coated separator and uncoated separator were calculated to be $1.054 \cdot 10^{-3}$ S cm^{-1} and $1.367 \cdot 10^{-4}$ S cm^{-1}, respectively. During battery cycling, the *d* of the CF-coated separator would become smaller, yet it would be still larger than that of the uncoated separator. Therefore, the κ_{eff} was higher in the CF-enabled battery, indicating that the polarization from the ohmic potential drop ($E_1^{\Delta s}$) was lower. On the other hand, practically, the κ_c is proportional to the square root of c_L (i.e., $\kappa_c = \alpha\sqrt{c_L}$, where α is a constant) [58], so the second term in equation (2) can be rewritten as

$$E_2^{\Delta s} = \frac{1}{j_{appl}}\left[-\int_0^{L^s} j_L \cdot \frac{2\alpha RT}{\sqrt{c_L}F} \cdot \frac{\partial c_L}{\partial x}\, dx\right] = \frac{1}{j_{appl}}\left[-\int_0^{L^s} j_L \cdot \frac{4\alpha RT}{F} \cdot \frac{\partial \sqrt{c_L}}{\partial x}\, dx\right] \quad (4)$$

where $\frac{\partial \sqrt{c_L}}{\partial x} \propto \frac{\partial c_L}{\partial x}$. Considering that the CF layer provided the extra kinetic energy, the ionic mobility was higher in the CF-enabled battery than that in the non-CF battery. Because of the higher mobility in the CF-enabled battery, the concentration gradient $\left|\frac{\partial c_L}{\partial x}\right|$ was lower, and so was the $\left|\frac{\partial \sqrt{c_L}}{\partial x}\right|$, leading to lower diffusion polarization. Due to the decrease in polarizations from both the ohmic potential drop and diffusion, consequently, the overall polarization induced by the CF-coated separator was much lower. Theoretically, the total polarization of a battery is calculated by adding all polarizations from different parts within the battery, which explains the relatively lower polarization voltage of the CF-enabled battery than that of the non-CF battery.

3.5 Sulfur distribution in batteries:

The cycled batteries were disassembled to determine how the CFs affected the distribution of polysulfides. SEM/EDS inspections were carried out on the APC/S cathode, Li anode, separator surface towards the cathode (separator@cathode), and separator surface towards the anode (separator@anode) (Figure 5a). The corresponding sulfur contents on the surfaces of individual components after cycling 10 times for the CF-enabled battery and non-CF battery are graphically summarized in Figure 5b. Comparing with the non-CF battery, the CF-enabled battery possessed a higher amount of sulfur on the cathode surface and separator@cathode, while less sulfur content was observed on the anode surface and separator@anode. This suggests that polysulfides were repelled by the CF-coated separator and remained at the cathode side in the CF-enabled battery. Moreover, the SEM image of the APC/S cathode surface in the CF-enabled battery after cycling 10 times (Figure 5c) shows pitting all over, which provided adequate spaces to load sulfur. This resulted in the sulfur content of 60.4 wt%. These pits were created by the CF layer due to the repelling behavior within the battery, and could also be observed on the cellulose fibers (Supporting information, Figure S10). In the non-CF battery, no pitting was found on the APC/S cathode surface after cycling 10 times (Figure 5d). This led to a lower sulfur content of 47.7 wt%. On the other hand, the Li anode surface of the CF-enabled battery (Figure 5e) after 10 cycles showed fewer sulfur-containing regimes (24.2 wt%) than that (37.7 wt%) of the non-CF battery (Figure 5f). The impurities on the separator@cathode (Supporting information, Figure S8 and S13) were found to be Ca-containing salts, which came originally from the CF coating and should have little impact on the electrochemical reaction [42, 43].

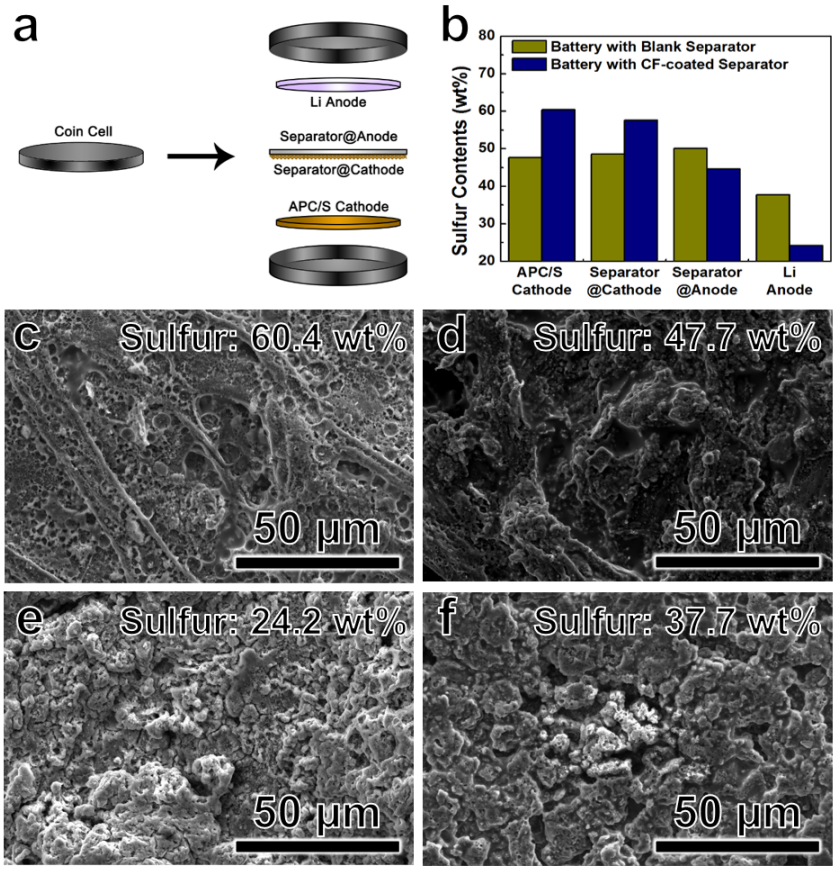

Figure 5. (a) Graphical constitute of a Li-S battery. (b) Sulfur contents on different surfaces after cycling 10 times. (c) SEM image of the APC/S cathode surface in the CF-enabled battery after cycling 10 times. (d) SEM image of the APC/S cathode surface in the non-CF battery after cycling 10 times. (e) SEM image of the Li anode surface in the CF-enabled battery after cycling 10 times. (f) SEM image of the Li anode surface in the non-CF battery after cycling 10 times.

3.6 Post-failure analysis of cycled batteries

The CF-enabled battery and non-CF battery failed after the 800th cycle and 466th cycle, respectively. Both batteries failed due to short circuiting, which was probably caused by the penetration of Li dendrites. Therefore, the longer lifespan of the CF-enabled battery is ascribed to the negatively charged CF-coated separator which inhibited Li dendrite growth by redistributing the Li-ions during cycling. SEM

inspection unveiled that local degradation of the Li anode in the non-CF battery (Figure 6b) was much more severe than that of the CF-enabled battery (Figure 6a). A similar conclusion can be made by comparing Figure 6c and 6d, where the red circles highlight the holes caused by the nonhomogeneous Li degradation on the Li anode in the non-CF battery. In contrast, no hole appeared on the Li piece in the CF-enabled battery. The optical inspection also revealed a more corroded Li anode in the non-CF battery (the inset of Figure 6d), and a relatively flat and intact Li anode in the CF-enabled battery (the inset of Figure 6c). The improved homogeneity of Li-ion distribution and degradation of the anode in the CF-enabled battery was enabled by the negatively charged CF layer redistributing Li-ions and repelling polysulfides. In addition, more pores and scratches caused by mossy Li were found on the non-CF separator than those on the CF-coated separator (Supporting information, Figure S9a and e, S10a and e, S13a and e, S14a and e, and S15), which also illustrates the more uniform Li distribution in the CF-enabled battery. The cathode in the CF-enabled battery kept its fiber structure (Supporting information, Figure S16a), yet the fiber structure was barely seen on the cathode surface in the non-CF battery (Supporting information, Figure S16b). In addition to more homogeneous distribution of Li-ions, the CF-enabled battery (Figure S17) demonstrated an suppressed polysulfide shuttle effect; lower sulfur content of 10.9 wt% was found on the cross section of the anode in the CF-enabled battery whereas higher sulfur content of 16.5 wt% was observed on the cross section of the anode in the non-CF battery.

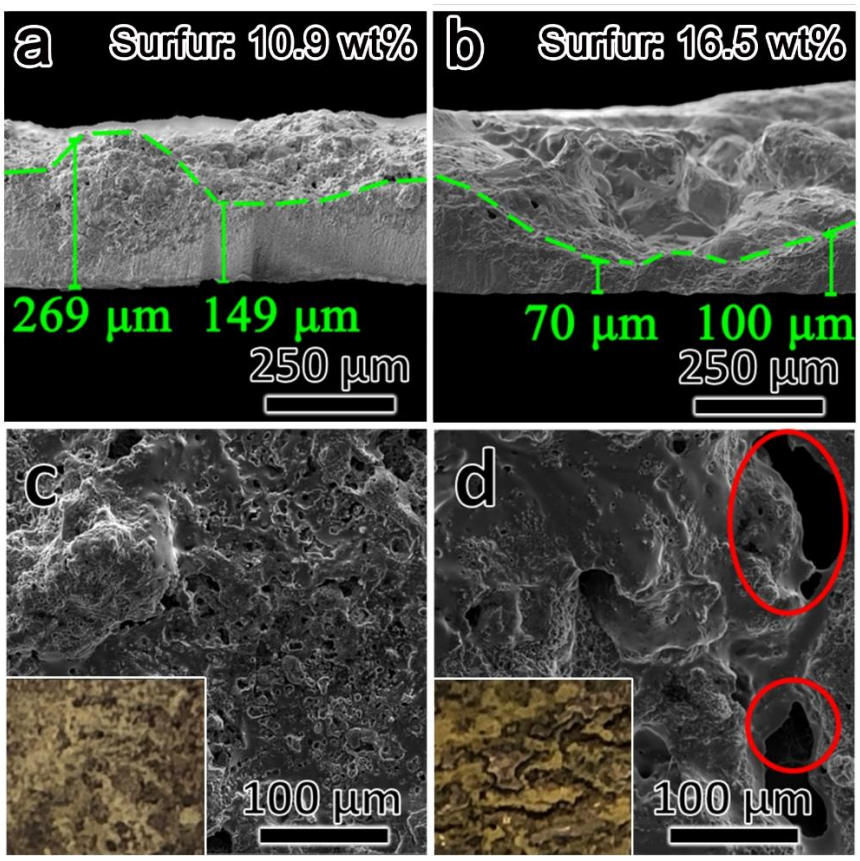

Figure 6. (a) SEM image of the Li anode cross section in the end-of-life CF-enabled battery. (b) SEM image of the Li anode cross section in the end-of-life non-CF battery. (c) SEM image of the Li anode surface in the end-of-life CF-enabled battery. The inset shows the optical image of the Li anode surface in the end-of-life CF-enabled battery. (d) SEM image of the Li anode surface in the end-of-life non-CF battery. The inset shows the optical image of the Li anode surface in the end-of-life non-CF battery.

4. Conclusions

Recycled paper hardboards were upcycled into CF-coated separators for Li-S batteries via a cost-effective method. The functional groups on CFs, including $-COO^-$ and $-C-O^-$, rendered a negatively charged surface which redistributed Li^+ and repelled S_x^{2-}, simultaneously mitigating the shuttle effect and mossy Li growth without

sacrificing the active materials. The CF-enabled battery exhibited good rate ability with a 72.43 % retention rate when the operation rate was octupled from 0.16 C to 1.28 C. The battery was cycled over 800 times with a capacity retention rate of 71.69 % at 0.5 C. The CF-enabled battery exhibited a smaller polarization than that of the non-CF battery due to the lower ohmic potential drop and diffusion polarization. The CF-coated separators are promising innovations to simultaneously overcome the two major challenges of Li-S batteries - the shuttle effect of polysulfides and nonhomogeneous degradation of Li. The readily accessible, renewable materials used in this study provide the large potential for the commercialization of low-cost, eco-friendly Li-S batteries.

Acknowledgement

Financial support for this study was provided by the U.S. National Science Foundation (CMMI- 1728042). The authors thank the staff members at the University of Virginia NMCF for electron microscopy technical support.

Conflict of Interest

The authors declare no conflict of interest.

Reference

[1] H. P. S. Abdul Khalil, A. H. Bhat, A. F. Ireana Yusra, Green composites from sustainable cellulose nanofibrils: A review, *Carbohydr. Polym.*, 2012, 87, 963-979.

[2] S. Osong, S. Norgren, and P. Engstrand, Processing of wood-based microfibrillated cellulose and nanofibrillated cellulose, and applications relating to papermaking: a review, *Cellulose*, 2016, 23, 93-123.

[3] M. Jonoobi, R. Oladi, Y. Davoudpour, K. Oksman, A. Dufresne, Y. Hamzeh, and R. Davoodi, Different preparation methods and properties of nanostructured cellulose from various natural resources and residues: a review, *Cellulose*, 2015, 22, 935-969.

[4] L. Mohammed, M. N. M. Ansari, G. Pua, M. Jawald, and M. S. Islam, A Review on Natural Fiber Reinforced Polymer Composite and Its Applications, *Int. J. Polym. Sci.*, 2015, 243947.

[5] I. Siró, and D. Plackett, Microfibrillated cellulose and new nanocomposite materials: a review, *Cellulose*, 2010, 17, 459-494.

[6] D. Boriboon, T. Vongsetskul, P. Limthongkul, W. Kobsiriphat, and P. Tammawat, Cellulose ultrafine fibers embedded with Titania particles as a high performance and eco-friendly separator for lithium-ion batteries, *Carbohydr. Polym.*, 2018, 189, 145-151.

[7] H. Zhang, J. Liu, M. Guan, Z. Shang, Y. Sun, Z. Lu, H. Li, X. An, and H. Liu, Nanofibrillated Cellulose (NFC) as a Pore Size Mediator in the Preparation of Thermally Resistant Separators for Lithium Ion Batteries, *ACS Sustainable Chem. Eng.*, 2018, 6, 4, 4838-4844.

[8] J. J. Zhang, Z. H. Liu, Q. S. Kong, C. J. Zhang, S. P. Pang, L. P. Yue, X. J. Wang, J. H. Yao, and G. L. Cui, Renewable and Superior Thermal-Resistant Cellulose-Based Composite Nonwoven as Lithium-Ion Battery Separator, *ACS Appl. Mater. Interfaces*, 2013, 5, 1, 128-134.

[9] J. Y. Hwang, H. M. Kim, S. Shin, and Y. K. Sun, Designing a High-Performance Lithium-Sulfur Batteries Based on Layered Double Hydroxides-Carbon Nanotubes Composite Cathode and a Dual-Functional Graphene-Polypropylene-Al_2O_3 Separator, *Adv. Funct. Mater.*, 2018, 28, 1704294.

[10] W. L. Cai, G. R. Li, K. L. Zhang, G. N. Xiao, C. Wang, K. F. Ye, Z. W. Chen, Y. C. Zhu, and Y. T. Qian, Conductive Nanocrystalline Niobium Carbide as High-Efficiency Polysulfides Tamer for Lithium-Sulfur Batteries, *Adv. Funct. Mater.*, 2018, 28, 1704965.

[11] Y. Zhong, L. Yin, P. He, W. Liu, Z. Wu, and H. Wang, Surface Chemistry in Cobalt Phosphide-Stabilized Lithium–Sulfur Batteries, *J. Am. Chem. Soc.*, 2018, 140, 4, 1455-1459.

[12] X. Liang, C. Hart, Q. Pang, A. Garsuch, T. Weiss, and L. F. Nazar, A highly efficient polysulfide mediator for lithium–sulfur batteries, *Nat. Commun.*, 2015, 6, 5682.

[13] A. Manthiram, S. H. Chung, and C. X. Zu, Lithium-Sulfur Batteries: Progress and Prospects, *Adv. Mater.*, 2015, 27, 1980-2006.

[14] Y. Zhang, Z. Gao, N. Song, J. He, and X. Li, Graphene and its derivatives in lithium–sulfur batteries, *Mater. Today Energy*, 2018, 9, 319-335.

[15] Y. Y. Zhang, F. M. Heim, N. N. Song, J. L. Bartlett, and X. D. Li, New Insights into Mossy Li Induced Anode Degradation and Its Formation Mechanism in Li-S Batteries, *ACS Energy Lett.*, 2017, 2, 2696-2705.

[16] J. Zhang, M. Huang, B. Xi, K. Mi, A. Yuan, and S. Xiong, Systematic Study of Effect on Enhancing Specific Capacity and Electrochemical Behaviors of Lithium–Sulfur Batteries, *Adv. Energy Mater.*, 2018, 8, 1701330.

[17] H. J. Peng, J. Q. Huang, X. B. Cheng, and Q. Zhang, Review on High-Loading and High-Energy Lithium–Sulfur Batteries, *Adv. Energy Mater.*, 2017, 7, 1700260.

[18] R. P. Fang, S. Y. Zhao, Z. H. Sun, D. W. Wang, H. M. Cheng, and F. Li, More Reliable Lithium-Sulfur Batteries: Status, Solutions and Prospects, *Adv. Mater.*, 2017, 29, 1606823.

[19] R. Elazari, G. Salitra, A. Garsuch, A. Panchenko, and D. Aurbach, Sulfur-Impregnated Activated Carbon Fiber Cloth as a Binder-Free Cathode for Rechargeable Li-S Batteries, *Adv. Mater.*, 2011, 23, 5641-5644.

[20] G. Q. Ma, Z. Y. Wen, M. F. Wu, C. Shen, Q. S. Wang, J. Jin, and X. W. Wu, A lithium anode protection guided highly-stable lithium-sulfur battery, *Chem. Commun.*, 2014, 50, 14209-14212.

[21] J. Q. Huang, Q. Zhang, and F. Wei, Multi-functional separator/interlayer system for high-stable lithium-sulfur batteries: Progress and prospects, *Energy Storage Mater.*, 2015, 1, 127-145.

[22] H. B. Yao, K. Yan, W. Y. Li, G. Y. Zheng, D. S. Kong, Z. W. Seh, V. K. Narasimhan, Z. Liang, and Y. Cui, Improved lithium-sulfur batteries with a conductive coating on the separator to prevent the accumulation of inactive S-related species at the cathode-separator interface, *Energy Environ. Sci.*, 2014, 7, 3381.

[23] Y.S. Su and A. Manthiram, A new approach to improve cycle performance of rechargeable lithium–sulfur batteries by inserting a free-standing MWCNT interlayer, *Chem. Commun.*, 2012, 48, 8817-8819.

[24] B. Zheng, N. Li, J. Yang, and J. Xi, Waste cotton cloth derived carbon microtube textile: a robust and scalable interlayer for lithium–sulfur batteries, *Chem. Commun.*, 2019, 55, 2289-2292.

[25] J. Yoo, S.J. Cho, G.Y. Jung, S.H. Kim, K.H. Choi, J.H. Kim, C.K. Lee, S.K. Kwak, and S.Y. Lee, COF-Net on CNT-Net as a Molecularly Designed, Hierarchical Porous Chemical Trap for Polysulfides in Lithium–Sulfur Batteries, *Nano Lett.*, 2016, 16, 5, 3292-3300.

[26] S. Li, G. Ren, M.N.F. Hoque, Z. Dong, J. Warzywoda, and Z. Fan, Carbonized cellulose paper as an effective interlayer in lithium-sulfur batteries, *Appl. Surf. Sci.*, 2017, 396, 28, 637-643.

[27] H. Yuan, T. Liu, Y. Liu, J. Nai, Y. Wang, W. Zhang, and X. Tao, A review of biomass materials for advanced lithium–sulfur batteries, *Chem. Sci.*, 2019, 10, 7484.

[28] M. Rana, M. Li, X. Huang, B. Luo, I. Gentle, and R. Knibbe, Recent advances in separators to mitigate technical challenges associated with re-chargeable lithium sulfur batteries, *J. Mater. Chem. A*, 2019, 7, 6596.

[29] J. Li, Y. Guo, P. Wen, J. Zhu, C. Jiao, L. Zhong, J. Wang, A.L. Narayana, J. Li, and Y. Qiu, Constructing a sandwich-structured interlayer with strong polysulfides adsorption ability for high-performance lithium-sulfur batteries, *Mater. Today Energy*, 2019, 14, 100339.

[30] C.H. Chang, S.H. Chung, S. Nanda, and A. Manthiram, A rationally designed polysulfide-trapping interface on the polymeric separator for high-energy Li–S batteries, *Mater. Today Energy*, 2017, 6, 72-78.

[31] Y. Y. Zhang, Z. Gao, and X. D. Li, Capillarity Composited Recycled Paper/Graphene Scaffold for Lithium-Sulfur Batteries with Enhanced Capacity and Extended Lifespan, *Small*, 2017, 13, 1701927.

[32] X. W. Yu, J. Joseph and A. Manthiram, Suppression of the polysulfide-shuttle behavior in Li-S batteries through the development of a facile functional group on the polypropylene separator, *Mater. Horiz.*, 2016, 3, 314.

[33] Y. Lu, S. Gu, J. Guo, K. Rui, C. H. Chen, S. P. Zhang, J. Jin, J. H. Yang, and Z. Y. Wen, Sulfonic Groups Originated Dual-Functional Interlayer for High Performance Lithium-Sulfur Battery, *ACS Appl. Mater. Interfaces*, 2017, 9, 14878-14888.

[34] T. Y. Lei, W. Chen, W. Q. Lv, J. W. Huang, J. Zhu, J. W. Chu, C. Y. Yan, C. Y. Wu, Y. C. Yan, W. D. He, J. Xiong, Y. R. Li, C. L. Yan, J. B Goodenough, and X. F. Duan, Inhibiting Polysulfide Shuttling with a Graphene Composite Separator for Highly Robust Lithium-Sulfur Batteries, *Joule*, 2018, 2, 2091-2104.

[35] P. Giannozzi, S. Baroni, N. Bonini, M. Calandra, R. Car, C. Cavazzoni, D. Ceresoli, G. L. Chiarotti, M. Cococcioni, I. Dabo, A. Dal Corso, S. De Gironcoli, S. Fabris, G. Fratesi, R. Gebauer, U. Gerstmann, C. Gougoussis, A. Kokalj, M. Lazzeri, L. Martin-Samos, N. Marzari, F. Mauri, R. Mazzarello, S. Paolini, A. Pasquarello, L. Paulatto, C. Sbraccia, S. Scandolo, G. Sclauzero, A. P. Seitsonen, A. Smogunov, P. Umari, R. M. Wentzcovitch, QUANTUM ESPRESSO: a modular and open-source software project for quantum simulations of materials, *J. Phys.: Condens. Matter*, 2009, 21, 395502.

[36] Y. Yao, and Y. Kanai, Plane-wave pseudopotential implementation and performance of SCAN meta-GGA exchange-correlation functional for extended systems, *J. Chem. Phys.*, 2017, 146, 224105.

[37] B. G. Pfrommer, M. Cote, S. G. Louie, M. L. Cohen, Relaxation of Crystals with the Quasi-Newton Method, *J. Comput. Phys.*, 1997, 131, 233-240.

[38] S. H. Kim, C. M. Lee, and K. Kafle, Characterization of crystalline cellulose in biomass: Basic principles, applications, and limitations of XRD, NMR, IR, Raman, and SFG, *Korean J. Chem. Eng.*, 2013, 30, 2127-2141.

[39] L. Hajji, A. Boukir, J. Assouik, S. Pessanha, J. L. Figueirinhas, M. L. Carvalho, Artificial aging paper to assess long-term effects of conservative treatment. Monitoring by infrared spectroscopy (ATR-FTIR), X-ray diffraction (XRD), and energy dispersive X-ray fluorescence (EDXRF), *Microchem. J.*, 2016, 124, 646-656.

[40] D. Dewi, H. Agusnar, Z. Alfian, and Tamrin, Characterization of technical kaolin using XRF, SEM, XRD, FTIR and its potentials as industrial raw materials, *J. Phys.: Conf. Ser.*, 2018, 1116, 042010.

[41] N. M. Julkapli, and S. Bagheri, Developments in nano-additives for paper industry, *J. Wood Sci.*, 2016, 62, 117-130.

[42] D. Aurbach, R. Skaletsky, and Y. Gofer, The Electrochemical Behavior of Calcium Electrodes in a

Few Organic Electrolytes, *J. Electrochem. Soc.*, 1991, 138, 12.

[43] M. Wang, C. Jiang, S. Zhang, X. Song, Y. Tang, and H.M. Cheng, Reversible calcium alloying enables a practical room-temperature rechargeable calcium-ion battery with a high discharge voltage, *Nat. Chem.*, 2018, 10, 667-672.

[44] W. Zhang, D. Liu, H. Lin, H. Lu, J. Xu, and D. Liu, On the cycling stability of the supercapacitive performance of activated carbon in KOH and H_2SO_4 electrolyte, *Colloids Surf., A*, 2016, 511, 294-302.

[45] B. Singh, Y. Fang, B. Cowie, L. Thomsen, NEXAF and XPS characterisation of carbon functional groups of fresh and aged biochars, *Org. Geochem.*, 2014, 77, 1-10.

[46] D. Briggs, and G. Beamson, XPS Studies of the Oxygen 1s and 2s Levels in a Wide Range of Functional Polymers, *Anal. Chem.*, 1993, 65, 1517-1523.

[47] J. McMurry, *Properties of Alcohols and Phenols*, Organic Chemistry Enhanced Edition, Eds. 7 (pp. 602–607), Belmont, 2009.

[48] M. Gu, J. Lee, Y. Kim, J. S. Kim, B. Y. Jang, K. T. Lee, and B. S. Kim, Inhibiting the shuttle effect in lithium–sulfur batteries using a layer-by-layer assembled ion-permselective separator, *RSC Adv.*, 2014, 4, 46940-46946.

[49] A. Schneider, J. Janek, and T. Brezesinski, Improving the capacity of lithium-sulfur batteries by tailoring the polysulfide absorption efficiency of hierarchical oxygen/nitrogen-functionalized carbon host materials, *Phys. Chem. Chem. Phys.*, 2017, 19, 8349.

[50] S. Bai, X. Liu, K. Zhu, S. Wu, and H. Zhou, Metal–organic framework-based separator for lithium–sulfur batteries, *Nat. Energy*, 2016, 1, 7, 16094.

[51] E. Peled, and S. Menkin, Review-SEI: Past, Present and Future, *J. Electrochem. Soc.*, 2017, 164, 7, A1703-A1719.

[52] Y. X. Lin, Z. Liu, K. Leung, L. Q. Chen, P. Lu, and Y. Qi, Connecting the irreversible capacity loss in Li-ion batteries with the electronic insulating properties of solid electrolyte interphase (SEI) components, *J. Power Sources*, 2016, 309, 221-230.

[53] Z. F. Deng, Z. A. Zhang, Y. Q. Lai, J. Liu, J. Li, and Y. X. Liu, Electrochemical Impedance Spectroscopy Study of a Lithium/Sulfur Battery: Modeling and Analysis of Capacity Fading, *J. Electrochem. Soc.*, 2013, 160, 4, A553-A558.

[54] R.P. Ramasamy, R.E. White, and B.N. Popov, Calendar life performance of pouch lithium-ion cells, *J. Power Sources*, 2005, 141, 298-306.

[55] A. Nyman, T. G. Zavalis, R. Elger, M. Behm, and G. Lindbergh, Analysis of the Polarization in a Li-Ion Battery Cell by Numerical Simulations, *J. Electrochem. Soc.*, 2010, 157, 11, A1236-A1246.

[56] B. Huber, L. Rossrucker, J. Sundermeyer, and B. Roling, Ion transport properties of ionic liquid-based polyelectrolytes, *Solid State Ion.*, 2013, 247-248, 15-21.

[57] Y. Zhang, J. He, Z. Gao, and X. Li, Converting eggs to flexible, all-solid supercapacitors, *Nano Energy*, 2019, 65, 104045.

[58] G. M. Roger, S. Durand-Vidal, O. Bernard, P. Turq, T. M. Perger, and M. Bester-Rogac, Interpretation of Conductivity Results from 5 to 45 °C on Three Micellar Systems below and above the CMC, *J. Phys. Chem. B*, 2008, 112, 16529-16538.

Supporting information

Upcycling of Paper Waste for High-performance Lithium-Sulfur Batteries

Yucheng Zhou [a], Yunya Zhang [a], Xiaodong Li [a], *

[a] Department of Mechanical and Aerospace Engineering, University of Virginia, 122 Engineer's Way, Charlottesville, VA 22904-4746, United States.

* Corresponding Author E-mail: xl3p@virginia.edu

Table S1. Comparison among recent work with polymer-based coatings on pp separators.

Coating Material	Coating Thickness (μm)	S Loading (mg cm^{-2})	Initial Capacity (mA h g^{-1})	Cycle Number	Decay Rate (per cycle)	Ref.
rGO-PVDF	130	1.1	1322	200	0.255 %	[1]
Nafion	1	0.53	781	500	0.080 %	[2]
Nafion	1-5	1.6	1100	110	0.410 %	[3]
g-PLiSS	25-32	2	1070	40	0.750 %	[4]
GO/Nafion	0.13	1.2	1128	200	0.210 %	[5]
SP/Nafion	3	1.5	859	250	0.190 %	[6]
PEG/MWCNT	25	3.9	1206	300	0.160 %	[7]
PAH/PAA	0.03	N/A	1418	50	1.400 %	[8]
Polydopamine	N/A	1.3	885	200	0.120 %	[9]
Polypyrrole	10	1.5	586	300	0.040 %	[10]
PAA-SWNT	7	2.7	770	200	0.120 %	[11]
PAN/GO	65	0.7-1	987	100	0.395 %	[12]
Our work	47.18	3.1	1016	**800**	**0.035 %**	

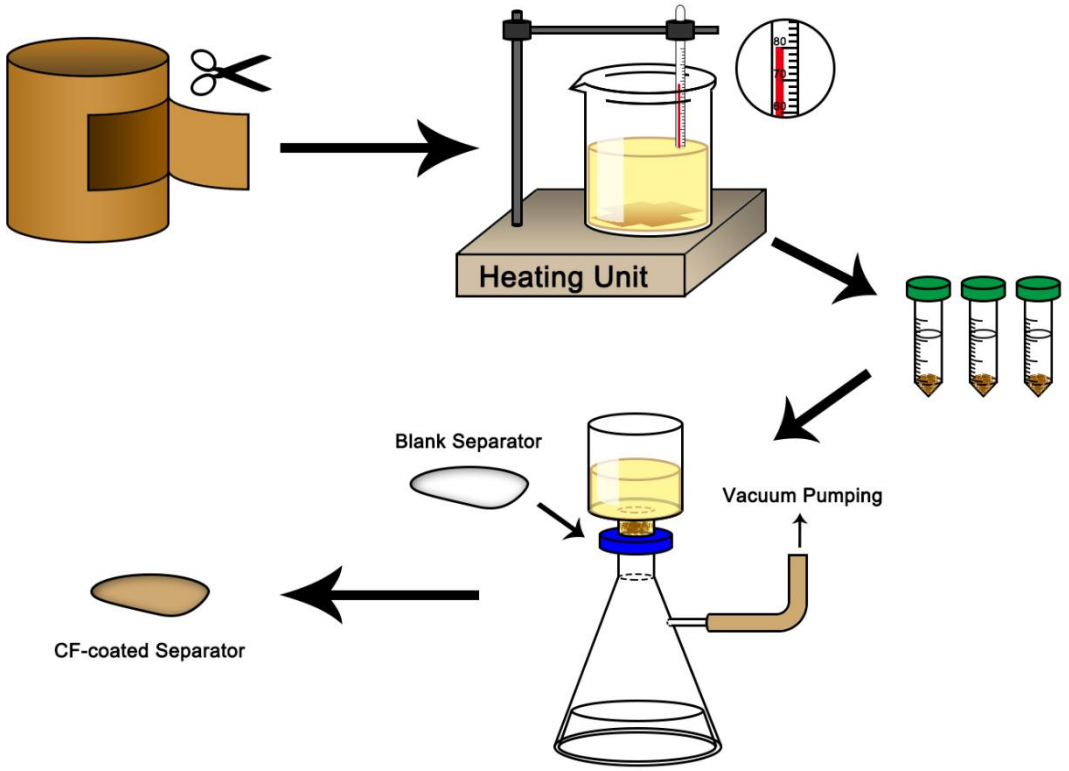

Figure S1. Experimental details of preparing CF-coated separators.

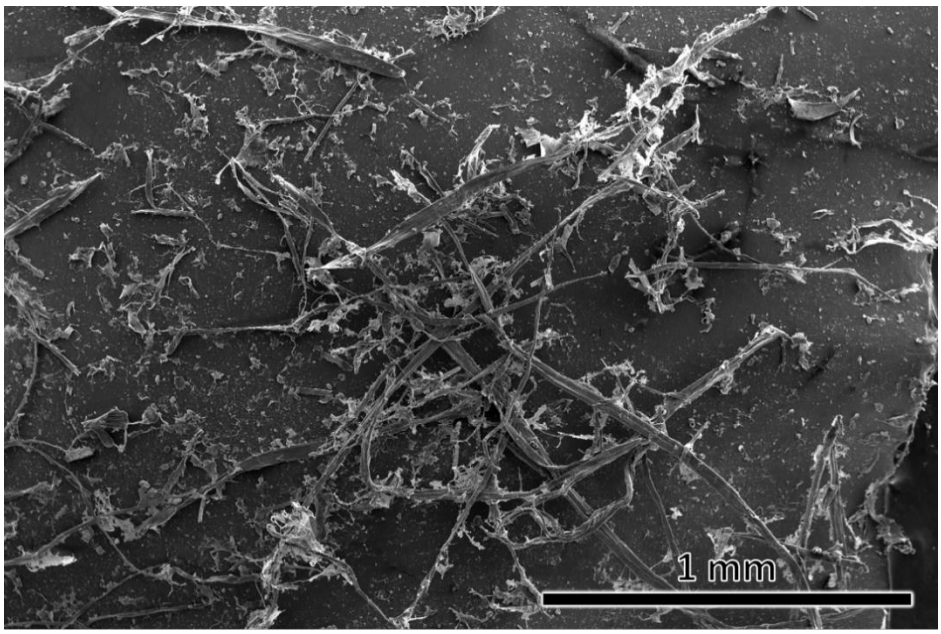

Figure S2. Low magnification SEM image of CFs.

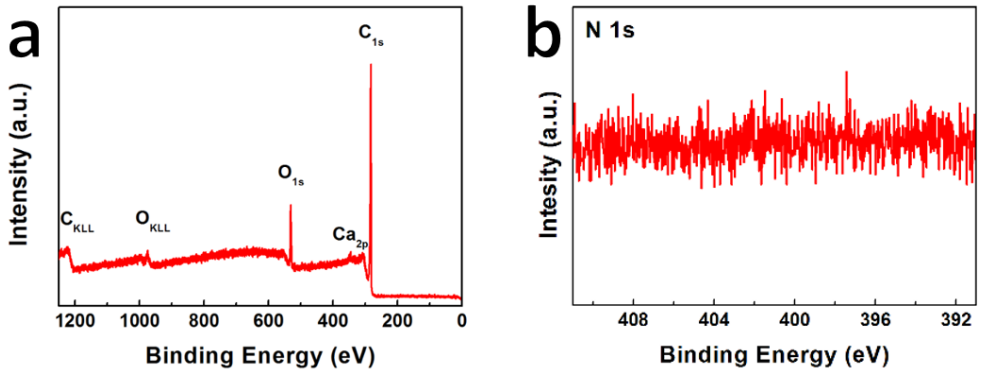

1

2 **Figure S3.** (a) Surface overall XPS spectrum. (b) N1s spectrum.

3

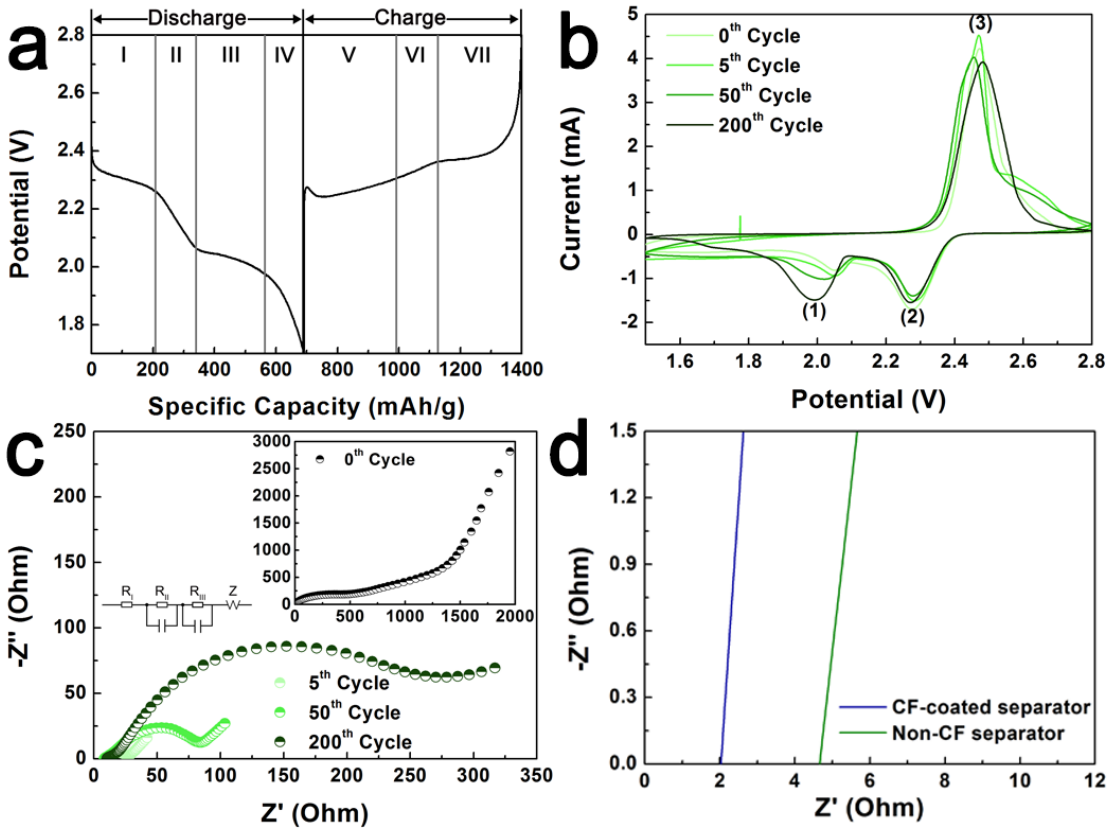

Figure S4. (a) Typical charge/discharge cycle of the non-CF battery. (b) CV curve of the non-CF battery. (c) EIS curve of the non-CF battery. The insets show the EIS curve of the battery before cycling and equivalent circuit of the EIS data. (d) EIS regression lines of the batteries with only electrolyte and a CF-coated separator or an uncoated separator.

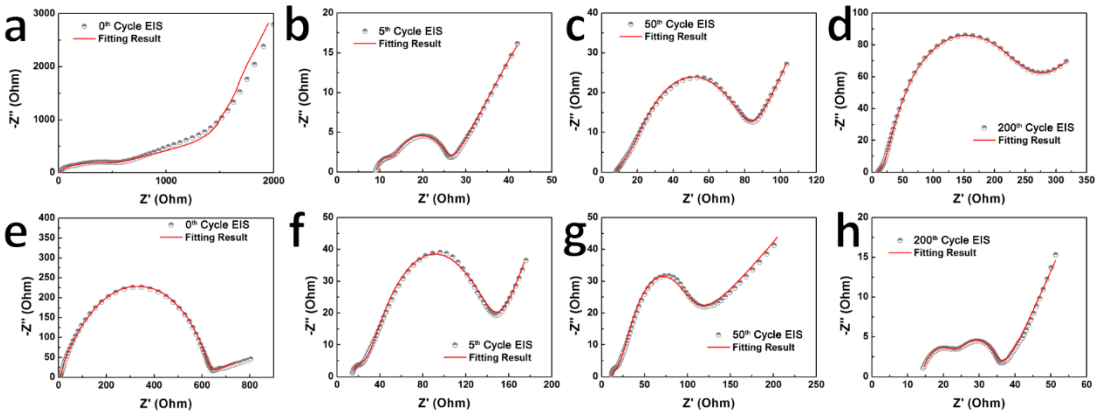

Figure S5. EIS curve fitting data for the non-CF battery at the (a) 0^{th} cycle, (b) 5^{th} cycle, (c) 50^{th} cycle, (d) 200^{th} cycle, and the CF-enabled battery at the (e) 0^{th} cycle, (f) 5^{th} cycle, (g) 50^{th} cycle, (h) 200^{th} cycle.

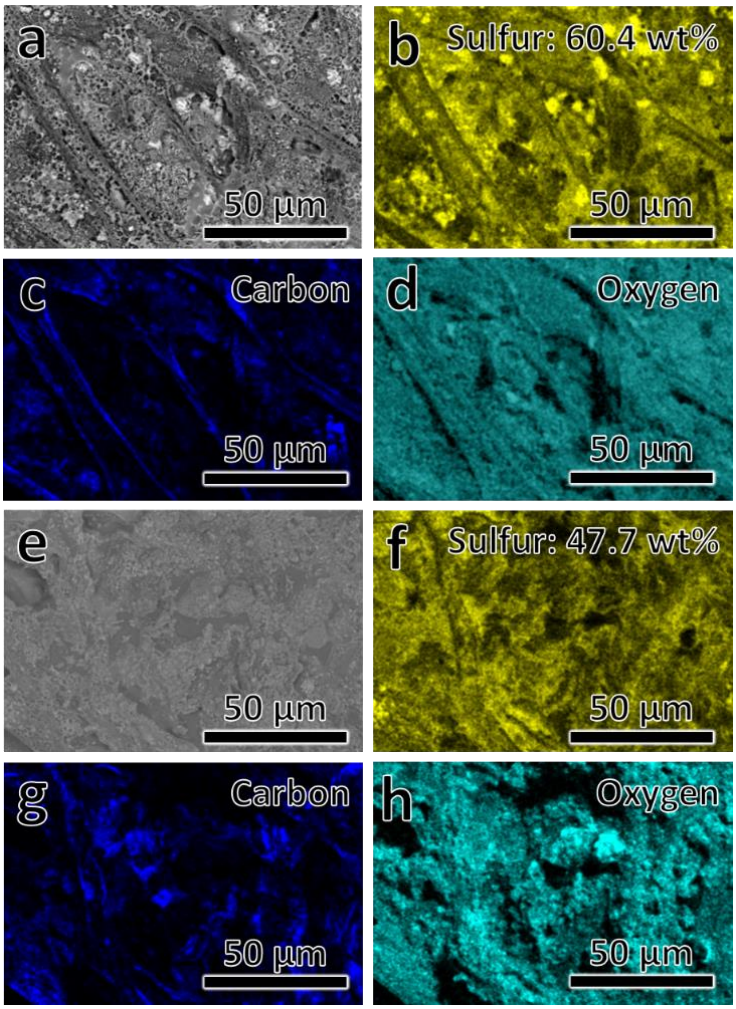

Figure S6. (a) SEM image, (b) EDS map of sulfur, (c) EDS map of carbon, (d) EDS map of oxygen of the APC/S cathode in the CF-enabled battery after cycling 10 times, and (e) SEM image, (f) EDS map of sulfur, (g) EDS map of carbon, (h) EDS map of oxygen of the APC/S cathode in the non-CF battery after cycling 10 times.

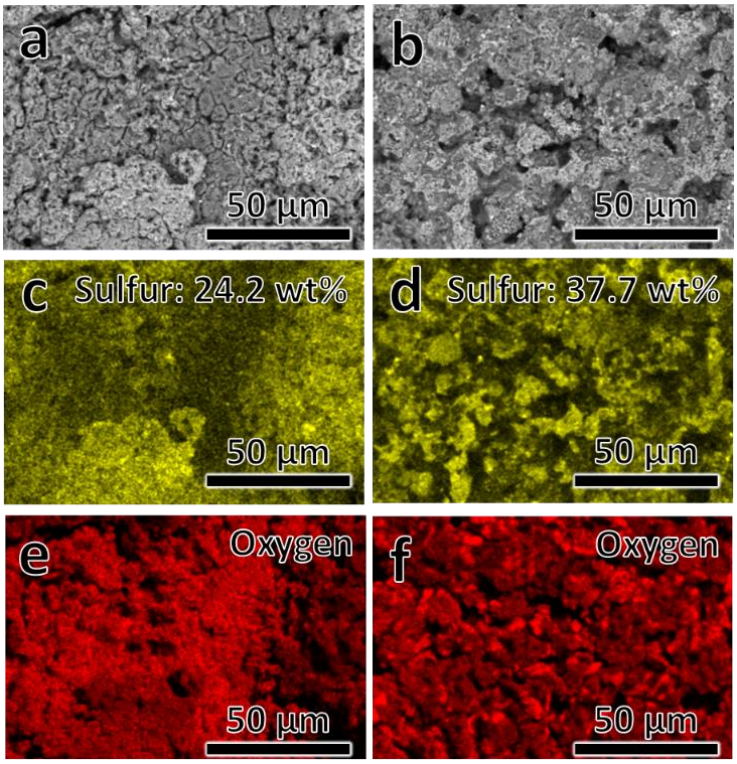

Figure S7. (a) SEM image, (c) EDS map of sulfur, (e) EDS map of oxygen of the lithium anode in the CF-enabled battery after cycling 10 times, and (b) SEM image, (d) EDS map of sulfur, (f) EDS map of oxygen for the lithium anode in the non-CF battery after cycling 10 times.

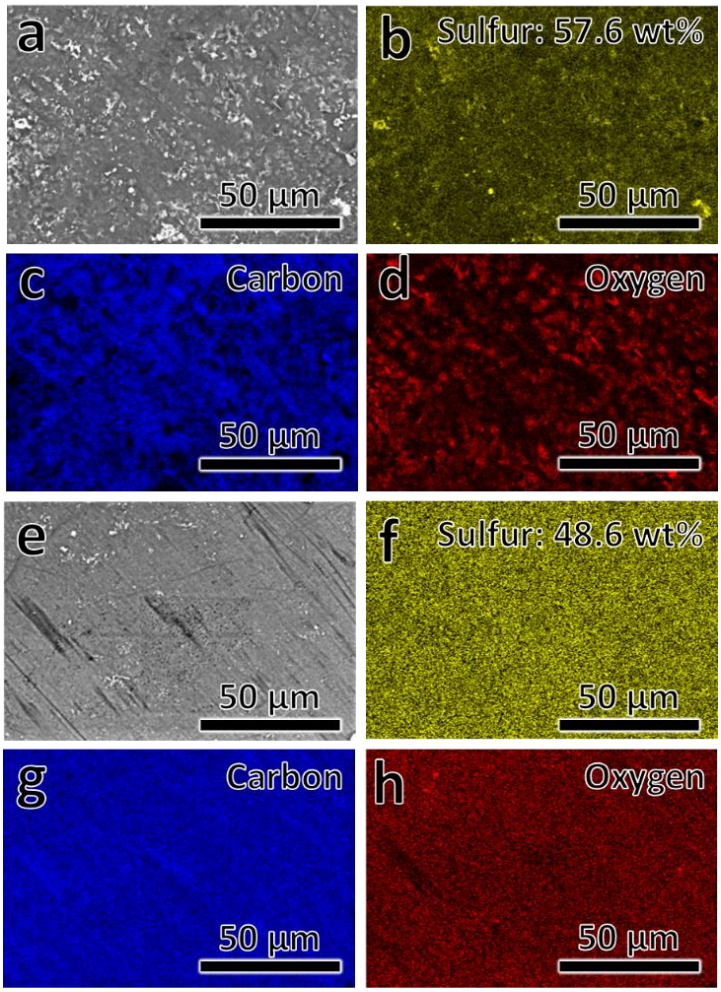

Figure S8. (a) SEM image, (b) EDS map of sulfur, (c) EDS map of carbon, (d) EDS map of oxygen of the separator towards the cathode in the CF-enabled battery after cycling 10 times, and (e) SEM image, (f) EDS map of sulfur, (g) EDS map of carbon, (h) EDS map of oxygen for the separator towards the cathode in the non-CF battery after cycling 10 times.

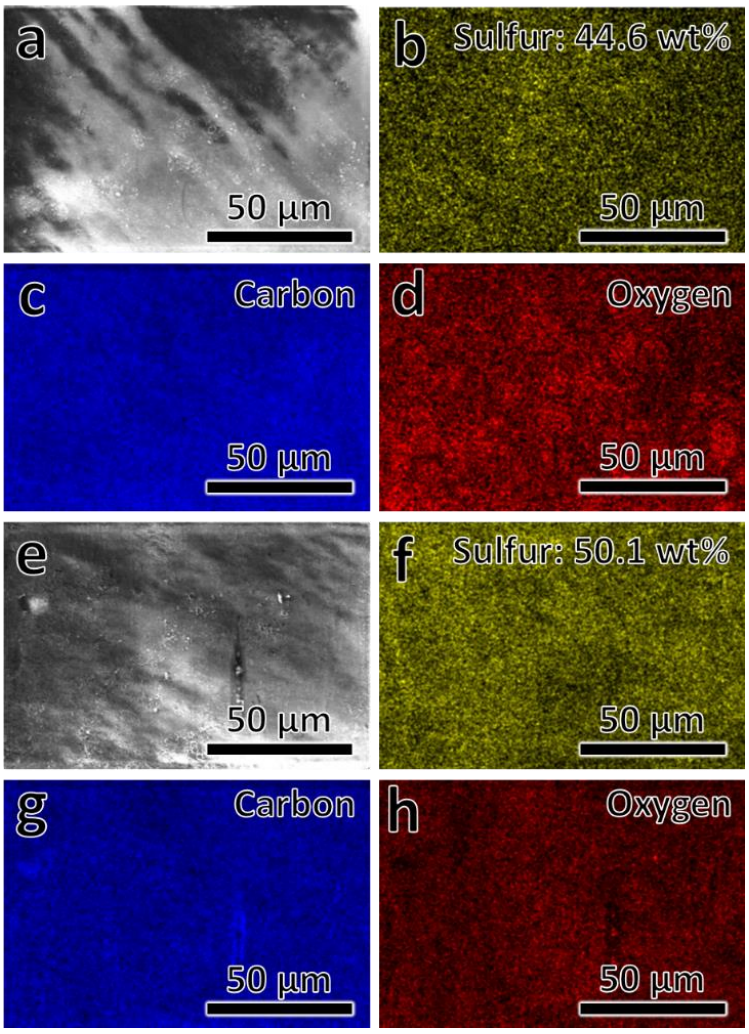

Figure S9. (a) SEM image, (b) EDS map of sulfur, (c) EDS map of carbon, (d) EDS map of oxygen for the separator towards anode in the CF-enabled battery after cycling 10 times, and (e) SEM image, (f) EDS map of sulfur, (g) EDS map of carbon, (h) EDS map of oxygen of the separator towards anode in the non-CF battery after cycling 10 times.

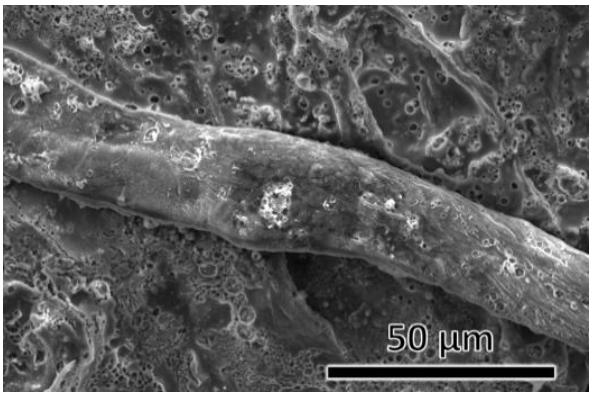

Figure S10. SEM image of the CF coating layer on the separator after cycling 10 times.

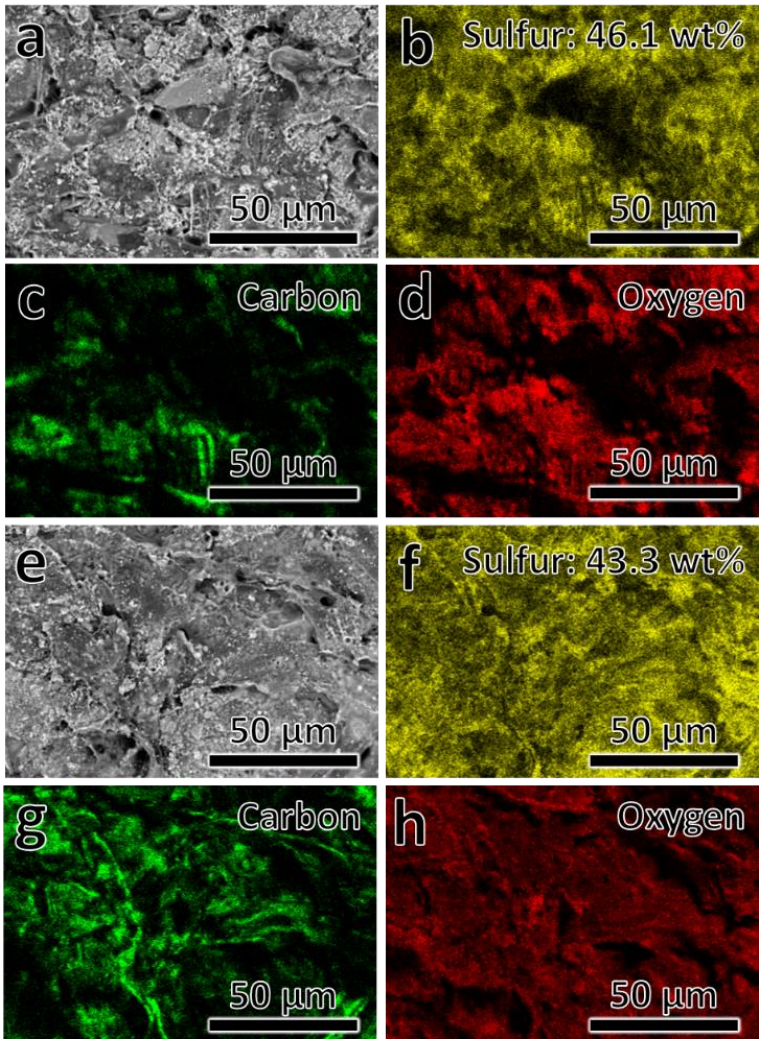

Figure S11. (a) SEM image, (b) EDS map of sulfur, (c) EDS map of carbon, (d) EDS map of oxygen of the APC/S cathode in the CF-enabled battery after cycling 100 times, and (e) SEM image, (f) EDS map of sulfur, (g) EDS map of carbon, (h) EDS map of oxygen of the APC/S cathode in the non-CF battery after cycling 100 times.

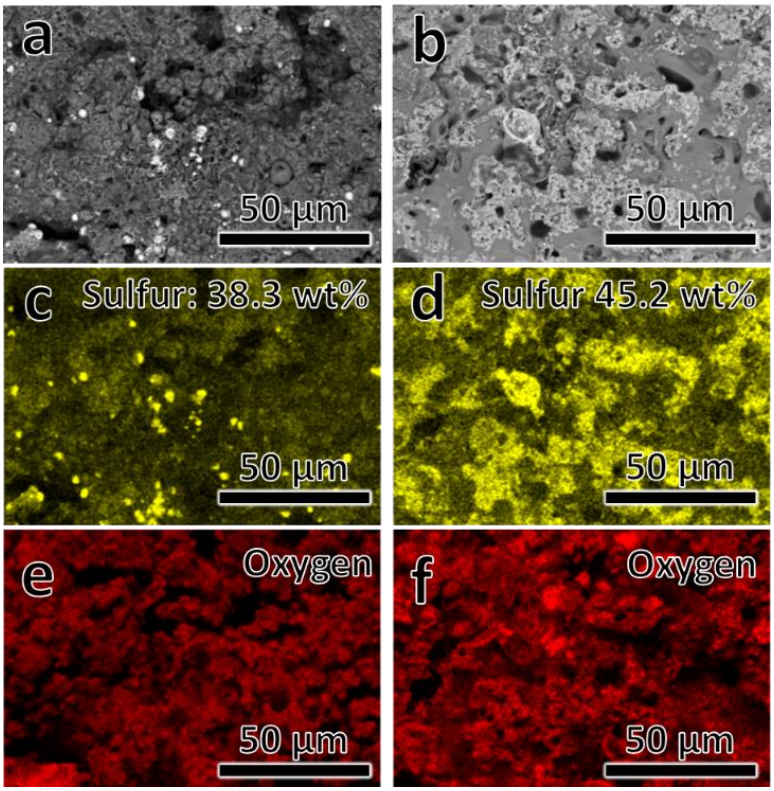

Figure S12. (a) SEM image, (c) EDS map of sulfur, (e) EDS map of oxygen of the lithium anode in the CF-enabled battery after cycling 100 times, and (b) SEM image, (d) EDS map of sulfur, (f) EDS map of oxygen of the lithium anode in the non-CF battery after cycling 100 times.

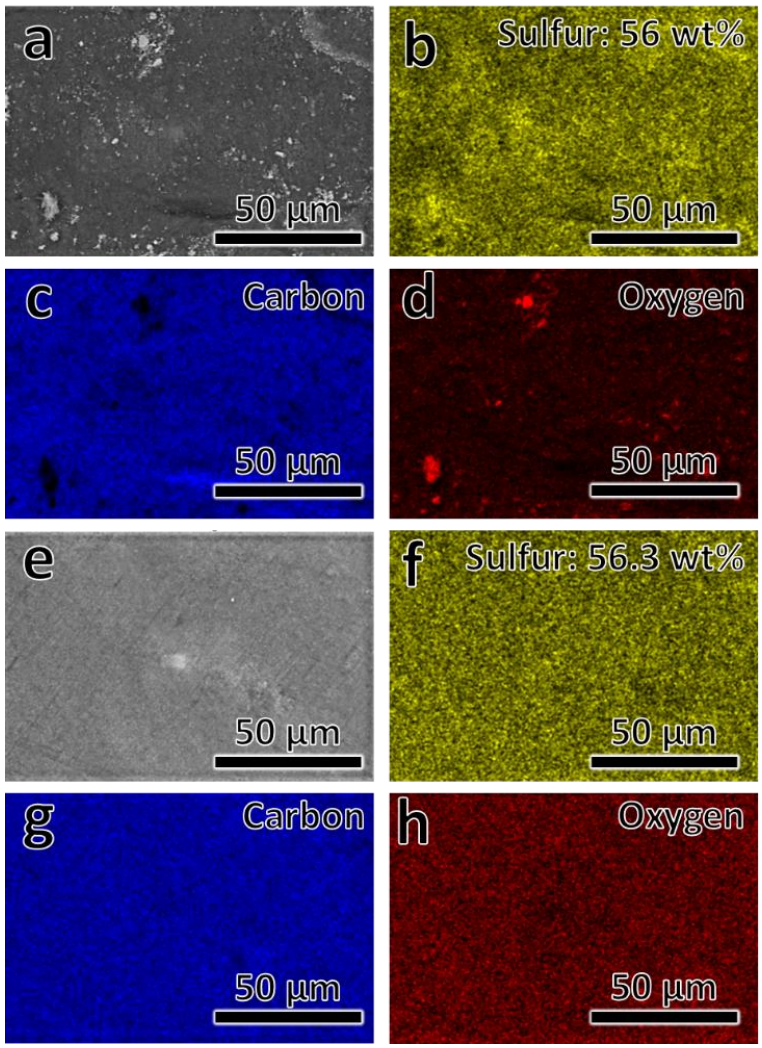

Figure S13. (a) SEM image, (b) EDS map of sulfur, (c) EDS map of carbon, (d) EDS map of oxygen of the separator towards the cathode in the CF-enabled battery after cycling 100 times, and (e) SEM image, (f) EDS map of sulfur, (g) EDS map of carbon, (h) EDS map of oxygen of the separator towards the cathode in the non-CF battery after cycling 100 times.

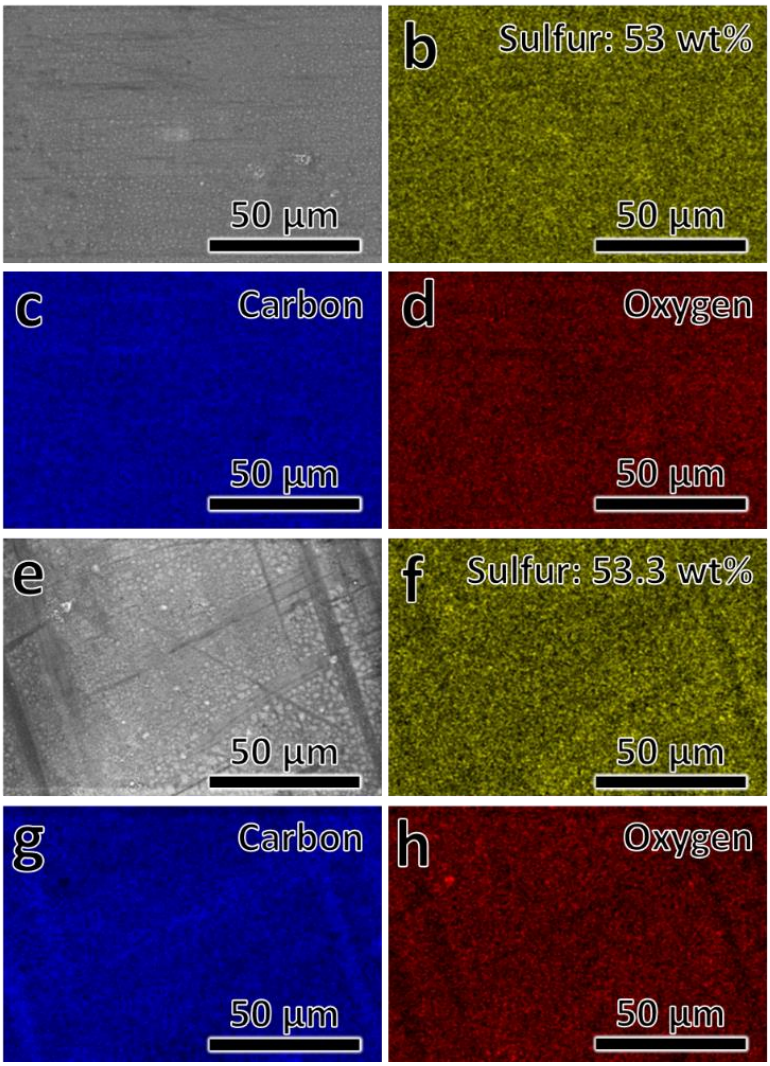

Figure S14. (a) SEM image, (b) EDS map of sulfur, (c) EDS map of carbon, (d) EDS map of oxygen for the separator towards anode in the CF-enabled battery after cycling 100 times, and (e) SEM image, (f) EDS map of sulfur, (g) EDS map of carbon, (h) EDS map of oxygen of the separator towards anode in the non-CF battery after cycling 100 times.

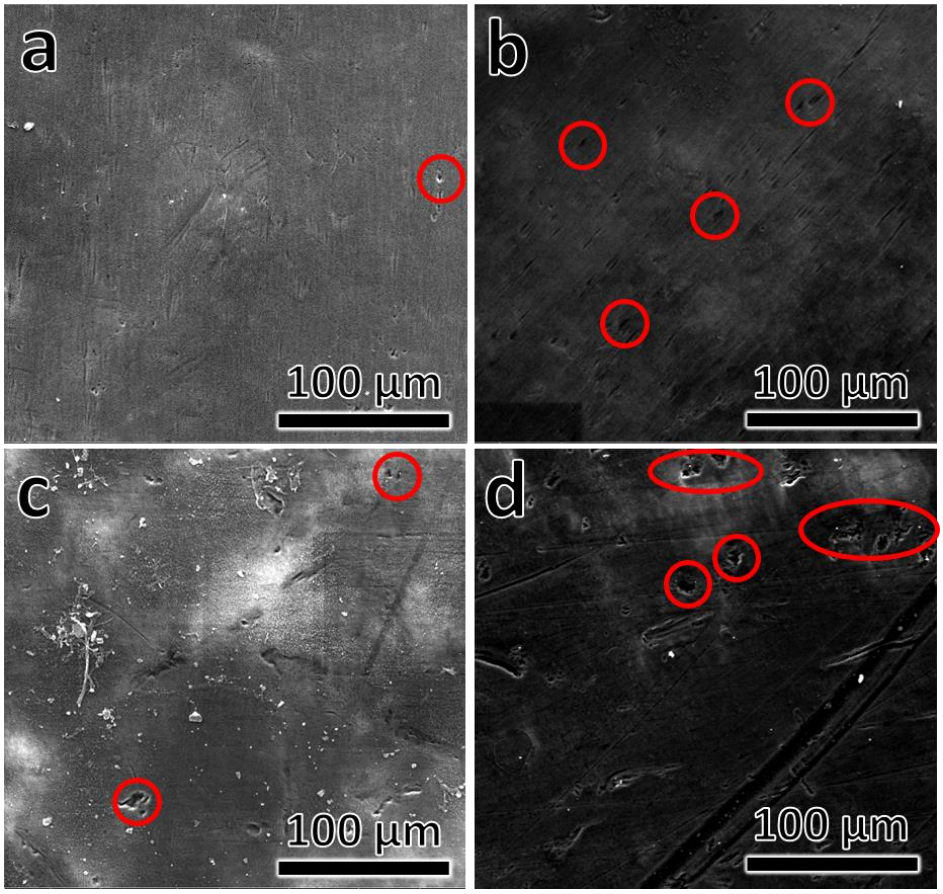

Figure S15. (a) SEM image of the separator surface facing the anode in the end-of-life CF-enabled battery. (b) SEM image of the separator facing the anode in the end-of-life non-CF battery. (c) SEM image of the separator surface facing the cathode in the CF-enabled battery. (d) SEM image of the separator surface facing the cathode in the non-CF battery.

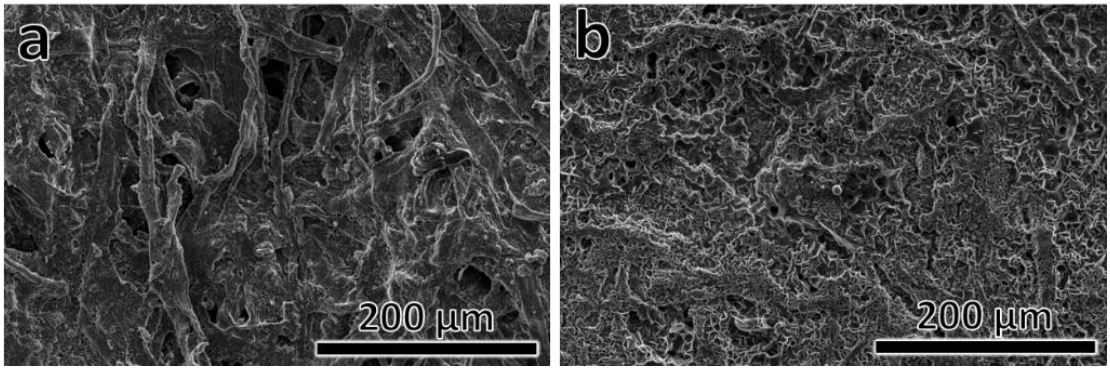

Figure S16. SEM images of the cathode in the end-of-life (a) CF-enabled battery, and (b) non-CF battery.

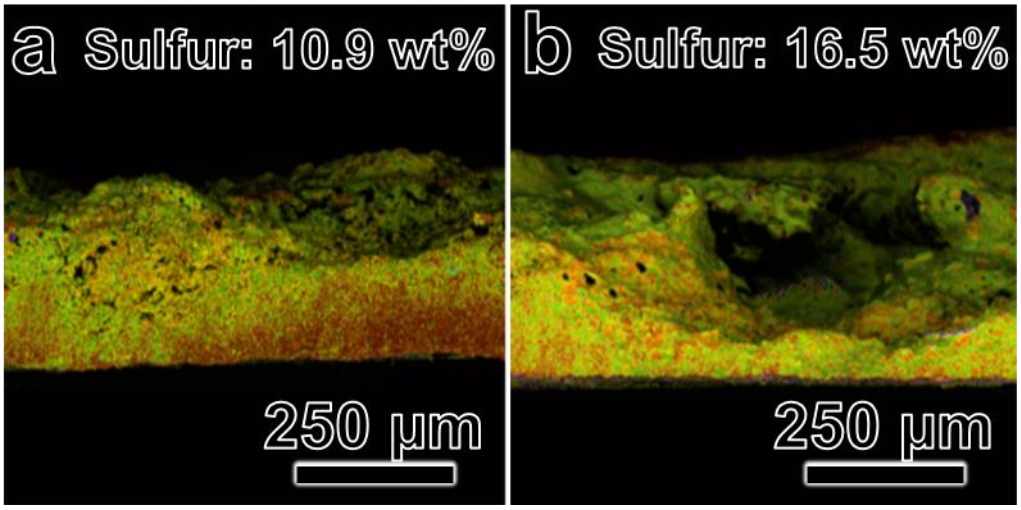

Figure S17. EDS maps of Li metal anode in (1) CF-enabled battery and (2) non-CF battery.

Reference

[1] P. Zhu, J. Zhu, J. Zang, C. Chen, Y. Lu, M. Jiang, C. Yan, M. Dirican, R.K. Selvan, and X. Zhang, A novel bi-functional double-layer rGO–PVDF/PVDF composite nanofiber membrane separator with enhanced thermal stability and effective polysulfide inhibition for high-performance lithium–sulfur batteries, *J. Mater. Chem. A*, 2017, 5, 15096-15104.

[2] J.Q. Huang, Q. Zhang, H.J. Peng, X.Y. Liu, W.Z. Qian, and F. Wei, Ionic shield for polysulfides towards highly-stable lithium–sulfur batteries, *Energy Environ. Sci.*, 2014, 7, 347.

[3] I. Bauer, S. Thieme, J. Bruckner, H. Althues, and S. Kaskel, Reduced polysulfide shuttle in lithium–sulfur batteries using Nafion-based separators, *J. Power Sources*, 2014, 251, 417-422.

[4] J. Conder, A. Forner-Cuenca, E.M. Gubler, L. Gubler, P. Novák, and S. Trabesinger, Performance-Enhancing Asymmetric Separator for Lithium–Sulfur Batteries, *ACS Appl. Mater. Interfaces*, 2016, 8, 29, 18822-18831.

[5] T.Z. Zhuang, J.Q. Huang, H.J. Peng, L.Y. He, X.B. Cheng, C.M. Chen, and Q. Zhang, Rational Integration of Polypropylene/Graphene Oxide/Nafion as Ternary‐Layered Separator to Retard the Shuttle of Polysulfides for Lithium–Sulfur Batteries, *Small*, 2016, 12, 381-389.

[6] Z. Hao, L. Yuan, Z. Li, J. Liu, J. Xiang, C. Wu, R. Zeng, and Y. Huang, High performance lithium-sulfur batteries with a facile and effective dual functional separator, *Electrochim. Acta*, 2016, 200, 197-203.

[7] L. Luo, S.H. Chung, and A. Manthiram, A trifunctional multi-walled carbon nanotubes/polyethylene glycol (MWCNT/PEG)-coated separator through a layer-by-layer coating strategy for high-energy Li–S batteries, *J. Mater. Chem. A*, 2016, 4, 16805-16811.

[8] M. Gu, J. Lee, Y. Kim, J.S. Kim, B.Y. Jang, K.T. Lee, and B.S. Kim, Inhibiting the shuttle effect in

lithium–sulfur batteries using a layer-by-layer assembled ion-permselective separator, *RSC Adv.*, 2014, 4, 46940-46946.

[9] Z. Zhang, Z. Zhang, J. Li, and Y. Lai, Polydopamine-coated separator for high-performance lithium-sulfur batteries, *J. Solid State Electrochem.*, 2015, 19, 1709-1715.

[10] G. Ma, Z. Wen, J. Jin, M. Wu, X. Wu, and J. Zhang, Enhanced cycle performance of Li–S battery with a polypyrrole functional interlayer, *J. Power Sources*, 2014, 267, 542-546.

[11] J.H. Kim, J. Seo, J. Choi, D. Shin, M. Carter, Y. Jeon, C. Wang, L. Hu, and U. Paik, Synergistic Ultrathin Functional Polymer-Coated Carbon Nanotube Interlayer for High Performance Lithium–Sulfur Batteries, *ACS Appl. Mater. Interfaces*, 2016, 8, 20092-20099.

[12] J. Zhu, C. Chen, Y. Lu, J. Zang, M. Jiang, D. Kim, and X. Zhang, Highly porous polyacrylonitrile/graphene oxide membrane separator exhibiting excellent anti-self-discharge feature for high-performance lithium–sulfur batteries, *Carbon*, 2016, 101, 272-280.